TU/e Department of Applied Physics
Fluids and Flows

NIOZ Department of Ocean Systems

Estimating time-dependent mesoscale mixing from moorings in the Irminger Sea

Author:
R. de Kreij

Supervisors NIOZ:
Dr. S. Groeskamp
Dr. M. F. de Jong

Supervisors TU/e:
Assistent Prof. M. Duran Matute
Prof. G.J.F. van Heijst

Eindhoven, September 29, 2020

R-2026-SE

Abstract

Mesoscale mixing (MM) takes place on large scales up to tens of kilometres and is an essential mechanism for distributing tracers such as heat, carbon, nutrients and oxygen throughout the entire ocean. Understanding of MM is necessary for improving numerical simulations of the ocean in climate systems. Within this study, the MM is derived from moorings by combining mixing length theory, mean-flow suppression theory and vertical eddy structures. We determine MM for seasonally, weekly and daily time scales, where we find strong intermittency of the MM on both weekly and daily time scales. This intermittency means a series of strong mixing bursts followed by periods of hardly any mixing. This intermittency has previously not been documented and is a novel insight gained through this project. The strength of the MM depends on the deformation radius, which represents the length scale over which a fluid parcel conserves its properties before mixing with its surrounding fluid. This deformation radius shows a clear variation throughout the seasons. Within this study, MM is estimated from moorings using different methods. One method, based on vertical velocity profiles, is the most accurate way to estimate MM. However, as velocity measurements are not globally available, we also compare this to an approximation using only vertical stratification. The use of the vertical stratification could be combined with altimetry, allowing for analyses of MM from global gridded climatologies rather than moorings.

Contents

Chapter 1

Introduction

Chapter Abstract

This chapter serves as an introduction to the report and starts with an explanation of the circulation in the Subpolar North Atlantic. This circulation is an essential element of the North Atlantic Ocean and has a significant influence on the global climate due to its large scale. The Irminger Current is part of this circulation and is located in the Irminger Sea. This Irminger Current is a double core current transporting warm and saline water in north-eastward direction. There are moorings deployed across the Irminger Current and the data from these moorings is used to estimate the mesoscale mixing. This chapter also explains the importance of the deducted study and states the relevant research questions required to estimate the mesoscale mixing.

1.1 Circulation in the Subpolar North Atlantic

The ocean's Meridional Overturning Circulation (MOC) is an essential element of the worldwide climate system [1]. In the Atlantic, the MOC is indicated as the Atlantic Meridional Overturning Circulation (AMOC) [2]. The AMOC consists of an upper and lower limb. The upper limb transports warm water in northward direction from the equator up to high latitudes [3]. Along its pathway, the water cools down and the salinity level decreases. The cooling down of the water causes the density to increase, while the loss in salinity causes the density to decrease. In total, the cooling down of the water dominates, causing the density to decrease. Due to the density decrease the water sinks into deeper layers of the ocean. The lower limb of the AMOC consists of the colder water in the deeper layers returning towards the equator [4]. The AMOC can be seen as the heat engine of the planet. Any significant disruption to the AMOC may lead to a change in heat distribution, which could lead to a change in climate [5, 6].

Figure 1.1 gives an overview of the currents around the North Atlantic subpolar gyre (NASPG) contributing to the AMOC. The North Atlantic Current (NAC) is the primary current of the AMOC upper limb. The NAC is a western boundary current in northeastward direction [7] and separates into two branches near the mid-Atlantic Ridge: the first branch flows in northeast direction into the Nordic seas, while the second branch circulates cyclonically around the Icelandic basin. This second branch flows southwest along the east side of the Reykjanes Ridge (RR), forming the East Reykjanes Ridge Current (ERRC) [8]. The ERRC loops around the RR, where it continues northwards as a start of the Irminger Current (IC). The IC circulates cyclonically around the Iriminger Sea (IS) [9] and collides with the East Greenland Current (EGC) near the east coast of Greenland, forming the Western Boundary Current (WBC). The WBC transports relatively cold and freshwater from the Greenland Sea [10]. The circulation ends a the Labrador Sea with the West Greenland Current (WGC) which enhances the Labrador Current (LC) going in southward direction [11].

Ocean currents can be separated into two categories: surface currents and non-surface currents. An example of a surface current is the Golf stream, which is visible from space using satellite data. However, the lower

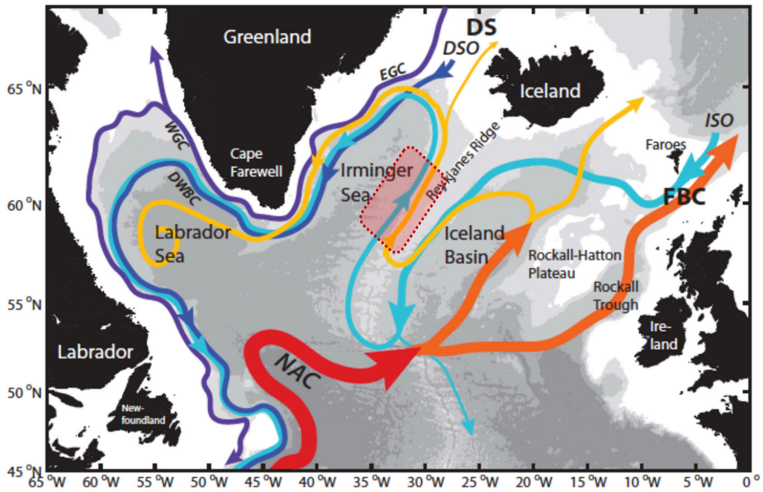

Figure 1.1: *Schematic overview of the major warm (red to yellow) and major cold (blue to purple) water flows in the North Atlantic subpolar gyre. The red box indicates the area of the IC. Within this area, the mesoscale mixing (MM) is estimated using mooring data. The horizontal and vertical axis respectively represent the longitude and latitude in degree [12].*

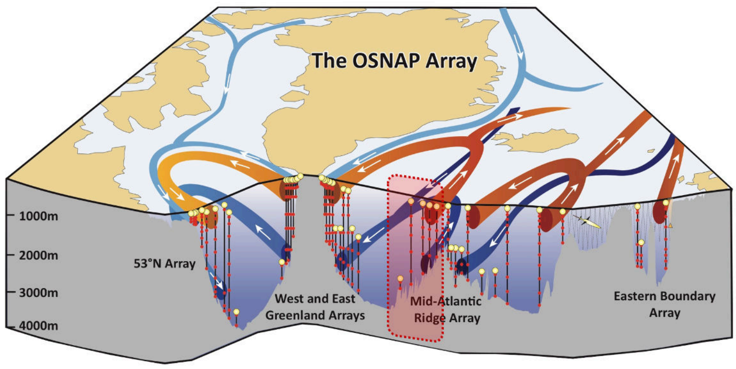

Figure 1.2: *Schematic overview of the OSNAP array. The black lines are the OSNAP moorings. The red dots are the measurement instruments attached to the moorings. The red box indicates the location of the IC array. The grey lines are the glider surveys. The red pathways indicate warm and salty transport of subtropical origin. The light blue pathways indicate fresh and cold surface waters of polar origin. The dark blue pathways indicate the water of high-latitude North Atlantic and Artic origin [12].*

limb of the AMOC is mostly hidden from satellites as it flows into the deeper layers of the ocean [5]; hence, it can not be measured using satellite data. Nevertheless, the AMOC can be measured using in situ instruments, such as moorings [8]. The circulation of the Subpolar North Atlantic is also studied using moorings, especially within the Overturning in the Subpolar North Atlantic Program (OSNAP), which is a program consisting of several international institutions observing the circulation over the whole North Atlantic since 2014 [12]. OSNAP is designed to provide a continuous recording of the full-water column, trans-basin fluxes of heat, mass and freshwater. The OSNAP array consists of 53 moorings to measure the AMOC, as shown in fig. 1.2. The OSNAP mooring array is divided into two zones: OSNAP West and OSNAP East. OSNAP West ranges from the southwestern tip of Greenland across the Labrador Sea to the southern Labrador. OSNAP East ranges from the southeastern tip of Greenland to Scotland [12]. NIOZ, the Royal Netherlands Institute for Sea Research, contributes to the OSNAP with five moorings located in the Irminger Sea across the IC. Within this study, these NIOZ moorings are used to estimate the mesoscale mixing (MM).

1.2 Irminger Current

The IC is a double core current located in the north Atlantic ocean. The IC flows in the northeastward direction towards Iceland on the west side of the RR [13], as shown in fig. 1.1. At the start of the IC it transports Subpolar Mode Water (SPMW) in the upper layers, which is relatively warm and saline water [14]. The SPMW originates from the Central Iceland Branch of the NAC [15] and cools down along the pathway of the IC where it sinks into deeper layers of the IS. The water mass underneath the SPMW is the North-East Atlantic Deep Water (NEADW), which is relatively colder and less saline [16]. The NEADW originates from the Iceland Scotland Overflow Water (ISOW) [8]. The NASPG also contains Labrador Sea Water (LSW), which is an intermediate water mass originating from the Labrador Sea. The LSW is located near the centre and east of the IS and has a relatively low salinity [12].

The IC contributes to the overturning of the North Atlantic subpolar gyre and flows cyclonically in the IS. When the IC approaches Iceland the current bends around the southwest coast, here, the IC separates in two currents: one current proceeds northward around Iceland, and the other current flows westward merging with the EGC [8, 12].

The IC consists of two cores: a western and an eastern core. The eastern core is relatively warmer and saltier, while the western core is more variable in terms of transport and location [17]. The mean total transport during 2014 - 2018 equals 10.4 ± 8.9 Sv, with the western core transporting 4.6 ± 6.8 Sv and the eastern core transporting 5.8 ± 5.4 Sv. As yet, the mooring data of the IC shows high daily and monthly variability of the current without a clear seasonal cycle [17].

1.3 Motivation of this study

The mixing of the ocean is of importance in the view of climate and ecosystems mechanics. The understanding of mixing is essential to track the transportation of tracers, such as heat, carbon, nutrient and oxygen. These transports play a significant role in the aspects of ocean warming, acidification and oxygenation. Which, in the end, influences the biodiversity and oxygen storage within the ocean [18].

MM is the mixing taking place on large scales up to tens of kilometres, but the effects are observed on even larger scales. Nevertheless, the time dependency of MM is a topic hardly discussed in literature. Before, MM was only analysed on a larger timescale of years 19. Within this study, the MM is analysed on shorter timescales in the order of days and weeks. The approach of analysing MM on a short timescale is a unique way of understanding MM. Including the intermittency effect may have broad influences on calculations of tracer fluxes. A clear understanding of MM and its intermittency is therefore required to improve the simulations of numerical models [20].

Further on, this study supports the general understanding of the IC in the IS, which contributes to the large scale AMOC [8]. The variability of the AMOC is expected to influence the regional and global climates due to its warm water transport in poleward direction [12]. There is a striving for a better understanding of the water, heat and salt transport throughout the years, to improve predictions of climate change [21].

1.4 Research questions

This section states the three main research questions. The first research question concerns the suppression effect of the MM. Suppression occurs when a mesoscale eddy and current propagate with a different velocity and/or direction, which results in an efficiency loss of the MM. Both the MM and suppression take place in horizontal dimensions, therefore in two dimensions. However, in literature, the suppression effect is approached as one-dimensional [22]. This one-dimensional approach assumes the mesoscale eddies to only propagate in zonal direction, with the suppression factor acting in the meridional direction. The suppression effect is also approached as an alternation of one-dimensional systems [19, 24], where the suppression is applied meridional or zonal, but not in a direction in between. The two-dimensional suppression effect is, however, not clearly defined in literature, which brings the first research question:

RQ 1: How should suppression of mesoscale mixing be interpreted in the horizontal plane?

The second research question is based on the timescale of MM. In literature, MM is approached as a time-dependent factor with a timescale of years [19]. However, MM can be determined on significantly shorter time scales using the mooring data. Estimating the MM on these short timescales is a new approach to MM, which brings the second research question:

RQ 2: What are the characteristics of a mesoscale mixing time series for a single water column?

Finally, the third research question is related to the method used to estimate MM. MM is initially estimated using the velocity measurements from the mooring data. Another approach would be to use first-surface modes, which allows the use of altimetry data instead of mooring data [19], which brings the third research question:

RQ 3: How does mesoscale mixing based on first-surface modes compare to mesoscale mixing based on direct velocity measurements?

The first research question is answered in chapter 2. The second and third research questions are answered in chapter 4.

1.5 This report

This report covers the following topics.

- In chapter 2 the theory is described, starting with the derivation of the MM. This derivation is based on mixing length theory, mean-flow suppression theory and vertical eddy structures.
- Chapter 3 describes the experimental setup. The chapter gives an overview of the used measurement instruments and the required data processing.
- Chapter 4 contains the results derived from the mooring data. The MM is analysed for different methods and timescales.
- Chapter 5 serves as conclusion and outlook, describing the remaining challenges and further research steps.

Chapter 2

Theory

Chapter Abstract

This chapter explains the derivation of the mesoscale mixing. The mesoscale mixing is initially estimated using the Mixing Length Theory, which assumes mesoscale eddies to propagate with the same velocity as the large scale mean flow. If however, an eddy propagates with a different velocity, then the mesoscale mixing is reduced as the eddy weakens due to shear stress. This reduction in mixing strength is known as suppression and is here derived using a one-dimensional system where both the eddy and the flow propagate in the zonal direction. The one-dimensional system is extended to a two-dimensional system, where the eddy and flow propagate in both the zonal and meridional direction. The mesoscale mixing is preferably estimated using vertical velocity profiles. However, as velocity measurements are not globally available, we also compare this to an approximation using only vertical stratification. The use of stratification could be combined with altimetry, allowing for analyses from global gridded climatologies rather than moorings.

2.1 Mixing Length Theory

The Mixing Length Theory (MLT) is used for a first estimation of the mesoscale eddy mixing in turbulent flows, as defined by [25, 26]:

$$K_{MLT} = \Gamma u_{rms} L_{mix}, \tag{2.1}$$

with K_{MLT} the mixing derived using the MLT in $\mathrm{m^2\,s^{-1}}$. Γ is the mixing efficiency, which is usually assumed to be an order-one constant [24]. L_{mix} is the mixing length scale in m, which is the characteristic length to which a fluid parcel conserves its properties before mixing with the surrounding fluid [27]. The MLT assumes that the eddy propagation speed is consistent with the propagation speed of the long Rossby waves; therefore the mixing length L_{mix} is set equal to the first Rossby deformation radius L_d [19]. u_{rms} is the root mean square (rms) velocity in $\mathrm{m\,s^{-1}}$, defined as

$$\begin{aligned} u_{rms} &= \sqrt{\left(U - \bar{U}^t\right)^2 + \left(V - \bar{V}^t\right)^2} \\ &= \sqrt{u'^2 + v'^2} \\ &= \sqrt{2EKE}, \end{aligned} \tag{2.2}$$

with U and V respectively the velocity in the longitudinal and latitudinal direction. u' and v' are the corresponding velocity variations of U and V. The EKE is the eddy kinetic energy in $\mathrm{m^2\,s^{-2}}$, which represents the kinetic energy of the time-varying component in the velocity field. For a single water column, the mixing

K_{MLT} depends on both time t and height z, as L_{mix} is a function of time and u_{rms} is a function of both time and height.

A mesoscale eddy causes particles in a current to mix in both the zonal (x) and meridional (y) directions. The eddy transport along the current is dominated by the mean current advection. Therefore, within this study, we only focus on the cross-current effective mixing $K_\perp$, as in this direction the transient eddies dominate [22]. The estimated mixing K_{MLT} is, however, not always equal to the effective cross-current mixing $K_\perp$, as a background flow could weaken the eddy. If there would be no background flow, then the eddies do not experience any shear by the flow; hence, the eddies remain their strength and diffusivity is maximized [24]. In addition, L_{mix} equals the eddy scale and the effective mixing $K_\perp$ equals K_{MLT}. However, if there would be a background flow, then an eddy is torn apart by the shear of the flow, causing the mixing length L_{mix} to reduce and the eddy to weaken [22]. The reduction in eddy strength induces a decrease of the effective mixing, which is known as suppression. The effect of suppression will be further illustrated in the next sections, starting from a one-dimensional diffusion mechanism.

2.2 One-Dimensional Mesoscale Mixing

This section explains the MM induced by an eddy on a current for a one-dimensional system. As the system is one-dimensional, both the mesoscale eddy and current propagate along the same or opposite direction. For now, the eddy and current only propagate along the zonal direction. A more realistic approach would be the two-dimensional MM, where both the eddy and current propagate in the zonal and meridional direction. The two-dimensional MM is derived using the one-dimensional MM mechanics, as further described in section 2.3.

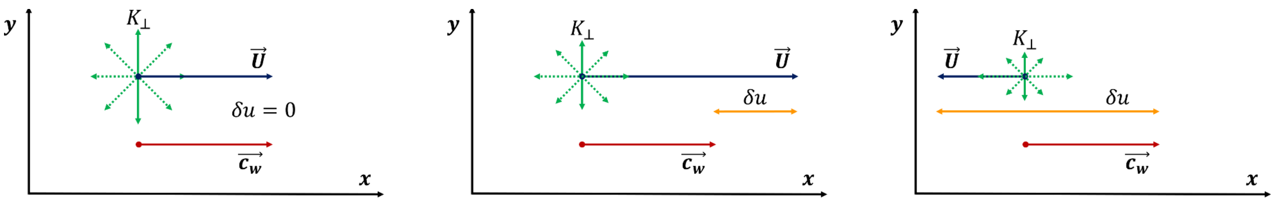

(a) *Eddy and current moving at the same speed.*

(b) *Eddy moving at a slower speed than the current.*

(c) *Eddy and current moving in opposite direction.*

Figure 2.1: *Plots of an eddy (red dot) propagating in positive x-direction (red arrow) with velocity $c_{w,x}$, located within a current (blue dot), propagating in the positive or negative x-direction (blue arrow) with current velocity U. The eddy causes mixing of the current (green arrows). The effective mixing component perpendicular to the current (solid green arrow) is indicated as $K_\perp$.*

Consider the systems of fig. 2.1, showing a current propagating with velocity U and a mesoscale eddy propagating with the Doppler-shifted eddy drift velocity $c_{w,x}$. There is assumed that the mesoscale eddies are transported by Rossby waves and by mean current advection [28]. Therefore, $c_{w,x}$ equals the propagation velocity of these Rossby waves plus the background advection $\bar{U}^{z,t}$, $c_{w,x}$ becomes

$$c_{w,x} = \bar{U}^{z,t} - \beta L_d^2 \tag{2.3}$$

for the one-dimensional system [29]. Here, β is the Rossby parameter, also known as the meridional derivative of the Coriolis parameter f. For the system of fig. 2.1a both the current and eddy propagate eastwards, therefore, the velocity difference $\delta u = c_{w,x} - U = 0$. Hence, there is no shear acting on the eddies, and these eddies are not torn apart by the current. The observed cross-current mixing $K_\perp$ occurs at the same strength as estimated from the MLT, thus $K_\perp = K_{MLT}$. For the system of fig. 2.1b the eddy moves slower than the current, therefore, the velocity difference $\delta u < 0$. Due to the velocity difference, the eddy observes friction with the current, which pulls the eddy apart as filaments from the eddies are peeled off. The effective mixing is reduced due to the weakened eddy. The cross-current mixing $K_\perp$ is thus suppressed and is weaker compared to the estimated MLT mixing, thus $K_\perp < K_{MLT}$. For the system of fig. 2.1c the eddy and current move in the opposite direction, resulting in an even larger shear velocity, which lowers the effective mixing even more due to the enhanced suppression.

The strength of the suppression can be derived from the one dimensional diffusion equation. This derivation starts with the mixing $K_\perp$ in meridional (y) direction, which is defined as follows:

$$K_\perp(x, y, t) = \lim_{t\to\infty} \int_0^t R\,(t', t)\, dt', \tag{2.4}$$

with R the autocorrelation of the meridional Lagrangian velocity [30], which equals

$$\begin{aligned} R\,(t', t) &= \langle \mathbf{v_L}(t : x, y, t) \cdot \mathbf{v_L}(t' : x, y, t)\rangle \\ &= \langle v_L(t : x, y, t) v_L(t' : x, y, t)\rangle \\ &= R_{vv}\,(t')\,, \end{aligned} \tag{2.5}$$

with R_{vv} the meridional term of the autocorrelation in $\mathrm{m\,s^{-2}}$ and $\mathbf{v_L}$ is the Lagrangian velocity in $\mathrm{m\,s^{-1}}$. The eddy field of the stochastic model is stationary, therefore, the autocorrelation R only depends on the difference t' and t:

$$R\,(t, t') = R\,(t - t')\,. \tag{2.6}$$

The Lagrangian velocity is equal to

$$\mathbf{v_L}(t' : x, y, t) = \mathbf{v}(x - Ut', y, t'), \tag{2.7}$$

with $\mathbf{v}$ the Eulerian velocity, which can be used in the autocorrelation as

$$R_{vv}\,(t') = \langle v\,(x - Ut', y, t')\, v(x, y, 0)\rangle\,. \tag{2.8}$$

An expression for v is determined using the quasi-geostrophic potential vorticity (QGPV) equation [29]:

$$\partial_t q + U\partial_x q + (\partial_y Q)\,\partial_x\psi + J(\psi, q) = 0, \tag{2.9}$$

with J the Jacobian, ψ the geostrophic streamfunction, and q the potential voriticity equal to $q = \nabla^2\psi - \psi L_d^2$. To solve the QGPV the following streamfunction (in terms of Fourier transform) is proposed:

$$\psi(x, y, t) = \frac{1}{2}\sum_k\sum_l a(t)e^{ikx+ily} + \text{c.c.}, \tag{2.10}$$

here, c.c. stands for the complex conjugate. The amplitude a is equal to

$$a(t) = \frac{2\mathcal{U}\sqrt{\gamma}}{\kappa}\int_0^\infty r(t - \tau)e^{-\gamma\tau - ikc_{w,x}\tau}d\tau, \tag{2.11}$$

with $\kappa^2 = k^2 + l^2$ the square of the total wavenumber and γ^{-1} the eddy decorrelation time scale. The decorrelation time scale γ^{-1} represents the eddy interaction time scale in the stochastic surface quasi-geostrophic model. γ^{-1} interacts with the time scale over which energy is transferred between waves of eq. (2.10) [22]. In turbulent fields, the eddy interaction time scale is proportional to the eddy strain rate of $\sqrt{2}(\kappa u_{rms})^{-1}$. Using this proportionality γ is rewritten to

$$\gamma = \frac{\kappa u_{rms}}{d_0\sqrt{2}}, \tag{2.12}$$

with d_0 a proportionality coefficient. Further on, there is assumed that the energy contained in the eddies is isotropic, and set κ equal to $\sqrt{2}k$. The wavenumber k is rewritten as $2\pi/L_d$, and γ is once more reduced to

$$\gamma = \frac{2\pi u_{rms}}{d_0 L_d}. \tag{2.13}$$

The velocity v is determined from eq. (2.10),

$$\begin{aligned} v\left(x - Ut', y, t'\right) &= \left.\frac{\partial\psi}{\partial x}\right|_{(x-Ut',y,t')} \\ &= \frac{1}{2} ika\left(t'\right) e^{ik\left(x-Ut'\right)+ily}, \end{aligned} \tag{2.14}$$

and is used to determine the autocorrelation of eq. (2.8):

$$R_{vv} = \frac{k^2 u_{rms}^2 \gamma}{\kappa^2}\left[\int_0^\infty d\tau' \int_0^\infty d\tau \left\langle r\left(t'-\tau'\right) r^*\left(t-\tau\right)\right\rangle e^{-\gamma\left(\tau+\tau'\right)+ik\left(c_{w,x}-U\right)\left(\tau-\tau'\right)} + \text{c.c.}\right], \tag{2.15}$$

here the c.c. is the complex conjugate of the preceding double integral. The autocorrelation R_{vv} is reduced with

$$\left\langle r\left(t'-\tau'\right) r^*\left(t-\tau\right)\right\rangle = \delta\left(t'-\tau'-t+\tau\right), \tag{2.16}$$

and so eq. (2.15) reduces to

$$R_{vv}\left(t'\right) = \frac{k^2 u_{rms}^2}{\kappa^2} e^{-\gamma t'} \cos\left[k\left(c_{w,x}-U\right)t'\right]. \tag{2.17}$$

The meridional mixing of eq. (2.4) becomes:

$$K_\perp = \frac{k^2}{\kappa^2}\frac{\gamma u_{rms}^2}{\gamma^2 + k^2\left(c_{w,x}-U\right)^2}. \tag{2.18}$$

When $c_{w,x} = U$, the eddies propagate with the same velocity as the flow itself, the mixing is then equal to K_{MLT}:

$$\begin{aligned} K_{MLT} &= \frac{k^2 u_{rms}^2}{\kappa^2\gamma} \\ &= \frac{u_{rms}^2}{2\gamma} \\ &= \frac{d_0 u_{rms} L_d}{4\pi} \\ &= \Gamma u_{rms} L_d, \end{aligned} \tag{2.19}$$

with the mixing efficiency Γ set equal to $d_0/4\pi$. The suppressed mixing $K_\perp$ is rewritten using K_{MLT}:

$$K_\perp = \frac{K_{MLT}}{1 + k^2\delta u^2/\gamma^2}. \tag{2.20}$$

The mixing $K_\perp$ can be expresses as K_{MLT} multiplied with a suppression factor $S_\perp$:

$$K_\perp = S_\perp K_{MLT} \tag{2.21}$$

$$S_\perp = (1 + k^2\delta u^2/\gamma^2)^{-1}. \tag{2.22}$$

The effective across-current mixing $K_\perp$ is the suppressed version of K_{MLT}. The suppression factor $S_\perp$ ranges from 0 up to and including 1. The strength of the suppression increases for decreasing L_d, decreasing γ or increasing δu.

2.3 Two-Dimensional Mesoscale Mixing

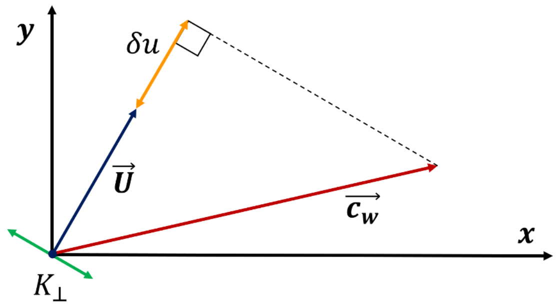

Figure 2.2: *Similar to fig. 2.1, but now for the two-dimensional MM system, where both the eddy and current propagate in x and y-direction.*

This sections explains the two-dimensional system for MM, as shown in fig. 2.2. In the previous section, the eddy and current propagated only in the zonal direction; however, in this section, the eddy and current have an additional meridional component. In two-dimensions the current velocity and the Doppler-shifted eddy drift velocity respectively become

$$\mathbf{U} = U\mathbf{e_x} + V\mathbf{e_y}, \tag{2.23}$$
$$\mathbf{c_w} = (\bar{U}^{z,t} - \beta L_d^2)\mathbf{e_x} + \bar{V}^{z,t}\mathbf{e_y}. \tag{2.24}$$

This two-dimensional system is more realistic compared to the one-dimensional system, as, for the moorings, the meridional velocity components of the eddy and current are of similar magnitude as the zonal components. Vertical velocities are neglected; therefore, the system does not have to be extended to three-dimensions.

As explained in section 2.2, the effective across-current mixing $K_\perp$ is a function of δu, which equals $c_{w,x} - U$ for the one-dimensional system. However, for the two-dimensional system, the value of δu is less straightforward. The across-current mixing $K_\perp$ requires the velocity difference δu between the current and the eddy in the direction of the current. δu is calculated by projecting $\mathbf{c_w}$ in the direction of the current $\mathbf{e_U}$. The value of δu is defined as following:

$$\begin{aligned} \delta u &= ||\mathbf{c_{w\|U}} - \mathbf{U}|| \\ &= \mathbf{c_w} \cdot \mathbf{e_U} - ||\mathbf{U}|| \\ &= \frac{c_{w,x}U + c_{w,y}V}{\sqrt{U^2+V^2}} - \sqrt{U^2+V^2} \\ &= \frac{(c_{w,x}-U)U + (c_{w,y}-V)V}{\sqrt{U^2+V^2}}, \end{aligned} \tag{2.25}$$

with $\mathbf{c_{w\|U}}$ the component of $\mathbf{c_w}$ projected on $\mathbf{U}$, and $\mathbf{e_U}$ the unit vector of $\mathbf{U}$. The suppressed mixing $K_\perp$ across the current is defined by eq. (2.20). δu of eq. (2.25) is verified for its one-dimensional limit cases: in the limit of $V = 0$ and $\mathbf{c_{w,y}} = 0$, δu equals $c_{w,x} - U$ which corresponds with section 2.2. In the limit case of $U = 0$ and $\mathbf{c_{w,x}} = 0$, δu equals $c_{w,y} - V$ which corresponds with literature [19]. The first research question RQ1 of section 1.4 is now answered, with the suppression factor defined by eq. (2.22).

2.4 First-surface modes

In previous sections the MM is derived using velocity measurements, however, as velocity measurements are not globally available, we also compare this to an approximation using only vertical stratification. The use of stratification could be combined with altimetry allowing for analyses from global gridded climatologies rather than moorings. This alternative method relies on first-surface modes, which are baroclinic (BC) modes that are obtained over steep or rough bathymetry [31]. These first-surface modes are derived from the linear quasi-geostrophic potential voriticity (QGPV) equation:

$$\frac{\partial}{\partial t}\left[\nabla^2\psi + \frac{\partial}{\partial z}\left(\frac{f^2}{N^2}\frac{\partial \psi}{\partial z}\right)\right] + \beta\frac{\partial \psi}{\partial x} = 0, \tag{2.26}$$

with $N(z)$ is the buoyancy frequency in s^{-1}, defined as:

$$N^2 = -\frac{g}{\rho_c}\frac{d\rho_0}{dz}, \tag{2.27}$$

with g the gravitational acceleration of the earth, $\rho_0(z)$ the background density and ρ_c the reference density of the water. The solutions of the linear QGPV equation are assumed to be wave-like in the horizontal plane, similar to section 2.2:

$$\psi(x, y, z, t) = \sum_{k,l,\omega} \phi(z)e^{ikx+ily-i\omega t}, \tag{2.28}$$

here $\phi(z)$ describes the vertical structure or mode of ψ. k and l are respectively the wavenumbers in the x and y-direction and ω the frequency. The wave-like solutions are substituted into eq. (2.26), resulting in the following differential equation [32]:

$$\frac{d}{dz}\left(\frac{f_0^2}{N^2}\frac{d\phi}{dz}\right) + \lambda^2\phi = 0, \tag{2.29}$$

with λ equal to:

$$\lambda^2 = -\left[k^2 + l^2 + \frac{\beta}{k\omega}\right]. \tag{2.30}$$

The derived modes of eq. (2.29) are used to estimate the Rossby deformation radius L_d, which equals

$$L_d = \frac{c_1}{|f|}, \tag{2.31}$$

with c_1 the eigenvalue of the first mode [33].

The vertical structure ϕ is derived by solving eq. (2.29). The boundary condition at the surface $z = 0$ is assumed to be rigid, so that the vertical velocity w and the vertical derivative of ϕ vanish [33]:

$$\left.\frac{\partial \phi}{\partial z}\right|_{(z=0)} = 0 \tag{2.32}$$

The boundary condition at the bottom $z = -H$ could be flat or rough. For a flat bottom the same boundary condition holds as at the surface:

$$\left.\frac{\partial \phi}{\partial z}\right|_{(z=-H)} = 0 \tag{2.33}$$

which is used for traditional baroclinic mode calculations [33]. The first flat bottom mode exhibits a clear zero crossing as shown in literature [33]. The other boundary condition, the rough bottom, is defined as following:

$$\phi(z = -H) = 0, \tag{2.34}$$

imposing that there is no flow at the bottom. The ϕ derived using a rough bottom boundary condition is also known as the first-surface mode. This mode decays monotonically from the surface to the bottom without changing sign [33]. To verify the correctness of the bottom condition (flat or rough), the vertical structure ϕ is compared with the dominating empirical orthogonal function (EOF) mode from current meter observations [32]. These EOF modes provide a simple representation of the vertical structure ϕ and can be derived using the mooring data. It has been shown that in almost the entire ocean the rough bottom boundary condition holds when assuming exponential stratification profiles [33]. Within this study, both the flat and rough bottom conditions are compared with the dominating EOF mode to determine which condition suits best. The comparison in boundary conditions is further discussed in section 4.5.

There are two different solution methods considered for solving eq. (2.28) for ϕ. The first solution method is the Wentzel-Kramers-Brillouin (WKB) approximation [34]. The WKB assumes an exponential wavefunction with a changing amplitude or phase. The other solution method is the Fourth-order Runge-Kutta (RK4) [35], which integrates downward from the surface from an initial guess, with adjustments to the eigenvalue made by using Newton's method until the bottom boundary condition is satisfied [33]. Here, the RK4 method utilizes the WKB solution as an initial guess. Within this study both solution methods are compared, there is, however, expected that the RK4 method is preferred due to its ability to solve complex stratification profiles numerically.

Finnally, eq. (2.28) is solved for ϕ using only the stratification N^2. Next, ϕ is used to determine u_{rms} as followig:

$$u_{rms} = \phi(z)\sqrt{2EKE_0}, \tag{2.35}$$

with EKE_0 the eddy kinetic energy at the surface, which can be measured using altimetry [19]. The required N^2 profiles can be obtained using the World Ocean Atlas (WOA) [19, 36] or using the mooring data. With this method u_{rms} can be determined without using any in situ velocity measurements, therefore, also the MM of section 2.3 can be estimated without the use of velocity measurements by moorings. Within this study, two methods to estimate MM based on first-surface modes are compared. One method uses first-surface modes derived from the WOA, and the other method uses first-surface modes derived from the stratification profiles of the moorings. In addition, these first-surface modes are compared with the velocity measurements of the moorings.

Chapter 3

Experimental setup

Chapter Abstract

This chapter describes the experimental setup used to derive the mesoscale mixing. The mesoscale mixing is calculated from moorings deployed across the Irminger Current. Different measurement instruments are used to measure velocity, temperature, salinity and pressure. The mooring data is filtered to remove tidal effects and data gaps are covered using regression coefficients and extrapolation. The vertical profiles per mooring are determined using interpolation to a partial Cartesian grid. A cross-section of the velocity, temperature, salinity and pressure of the Irminger Current is determined by horizontally interpolating these vertical profiles.

3.1 Mooring deployment

The conducted study uses observations from moorings. A mooring is a collection of measurement instruments connected to a wire with an anchor on the seafloor. The mooring is kept straight by buoys on top. The top of the mooring remains below the water surface to protect the mooring against fishing nets, rough weather conditions and collisions with ships. A mooring is recovered by triggering its releases, which disconnect the mooring from its anchor, causing the mooring to float to the surface. The figs. 3.1 and 3.2 show one of the research vessels used to recover, service and redeploy the moorings. An essential advantage of mooring measurements is the ability to measure with a high temporal resolution. Other advantages are the ability to measure at great depths and to measure with an accuracy better than satellites. Further on, a cross-section of the ocean could be analysed by deploying multiple moorings as an array.

There are five moorings deployed by NIOZ across the IC on the west side of the Reykjanes Ridge, as shown in fig. 3.3. A vertical cross-section of the mooring array is shown in fig. 3.4. These moorings are used to study the variability of the IC [8, 17]. The deployed moorings provide high temporal resolution, full-depth, year-round observations of temperature, salinity and velocity. These moorings are highly suited for studying MM of a single water column on short time scales due to the near-continuous, full water column observations [8].

Table 3.1: *Overview of mooring deployment positions and bottom depths.*

Mooring ID	Latitude (°N)	Longitude (°W)	Bottom depth (m)
IC0	59°12.88′	35°07.55′	2938
IC1	59°05.93′	33°40.93′	2509
IC2	59°01.23′	32°46.05′	1978
IC3	58°57.33′	31°57.54′	1635
IC4	58°53.12′	31°18.18′	1477
M1	58°52.33′	30°31.95′	1712

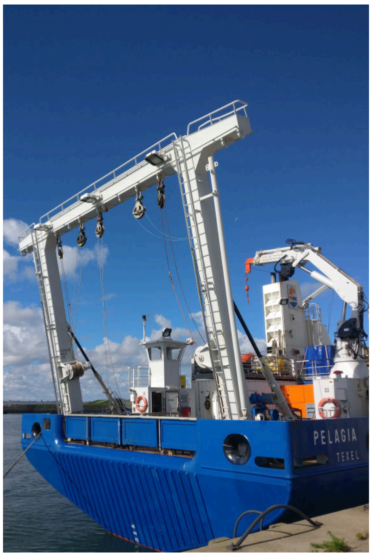

Figure 3.1: *Picture of the A-frame on the back of the Research Vessel (RV) Pelagia used to deploy and recover the moorings. The RV Pelagia is runned by NIOZ.*

Figure 3.2: *Picture of mooring recovery. The left orange buoy contains the ADCP. The yellow buoys serve as extra buoyancy. Both types of buoys are part of the upper section of the mooring. Photo credits: Nora Fried.*

The moorings are labelled from west to east as IC0, IC1, IC2, IC3 and IC4. Table 3.1 shows the mooring locations and bottom depths. The moorings are positioned in a straight line and cover a distance of 222 km. The moorings IC1 to IC4 are tall moorings covering the entire water column. The most western mooring IC0 is a short mooring, covering only the lower section of the foot of the Reykjanes Ridge from the bottom, at 2938 m, to 2250 m depth. IC0 is used to capture the variability of the North-East Atlantic Deep Water (NEADW). A complete profile of the water column is required to estimate MM; therefore, IC0 is not used to estimate the MM. The four tall moorings IC1 to IC4 are located on the flank of the ridge. IC4 is the shallowest mooring as it is positioned on top of the ridge, with a bottom depth of 1477 m. The difference in bottom depth between the deepest and shallowest mooring equals 1461 m. The average bottom slope of the IC moorings equals 6.58 m km^{-1}. An additional American mooring M1 is added to the analysis, which is positioned on the East side of the RR, as shown in fig. 3.3. The measurements of M1 are initially used to determine the border between the IC and the ERRC. The IC moorings and M1 cover a total distance of 267 km, with an average spacing of 37 km per mooring.

The moorings were deployed for the first time during the summer of 2014 and have been serviced in 2015, 2016, 2018 and 2020. For this study, a total of 4 years of mooring data is used to estimate the MM, starting from 13/07/2014 up to and including 15/07/2018. During this period the moorings have been serviced twice, resulting in two data gaps: the first gap is during 29/06/2015-16/07/2015 and second gap during 18/06/2016-12/08/2016. Subtracting these data gaps leaves a total of 1422 measurement days.

3.2 Measurement Instruments

This section describes the used measurement instruments [8] attached to the moorings, as shown in fig. 3.4. For the IC moorings the velocity is measured by two types of current meters: multi-point and single point. Multi-point measurements are done by the Acoustic Doppler Current Profiler (ADCP). An ADCP sends an acoustic signal which reflects due to the particles within the water column. The reflected signal is captured by the ADCP and translated into velocities using the Doppler effect. The IC moorings use the ADCP RDI

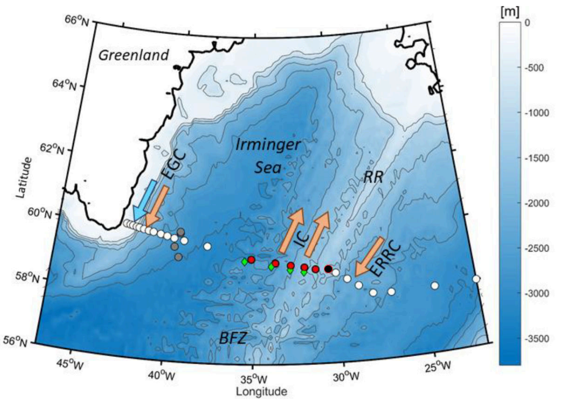

Figure 3.3: *Schematic overview of currents, bathymetry and moorings in the Irminger Sea. The indicated currents are the double core IC, the East Greenland Current (EGC) and the East Reykjanes Ridge Current (ERRC). Two main topographic elements are the Reykjanes Ridge (RR) and the Bight Fracture Zone (BFZ). Red dots are the IC moorings IC0 (west) up to and including IC4 (east). White dots are the other OSNAP moorings. Black dot is the M1 mooring. Green diamonds are the positions of the LOCO moorings. The grey dots are central Irminger Sea moorings [8].*

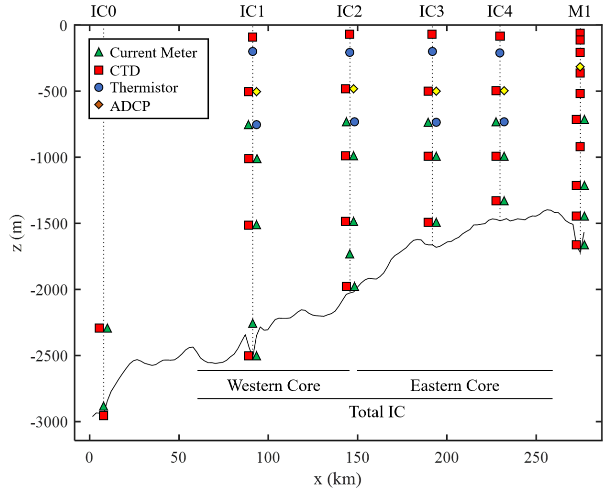

Figure 3.4: *Schematic overview of instrument depths. Black line is the bottom topography, dotted black lines are the moorings lines, green triangles the current meters, blue spheres the thermistors and the oranges diamonds the ADCP [17].*

75 kHz Long Ranger. The ADCPs are only attached to the tall moorings at a target depth of 475 m and are looking upward. The ADCP's measure up to 50 m depth below the surface, with a sample interval of 1 hour.

The single point measurements are done by RCM11's and Aquadopps. RCM stands for Rotating Current Meter. However, the RCM11 is not actually an RCM, as it does not have any rotating element. Both the RCM11's and Aquadopps use the Doppler effect to measure the current velocity at a single depth. For the tall moorings the single point current meters are attached at target depths of 725, 950, 1450, 2250 and 50 m above the bottom. The sample interval of the current meters is set to 20 or 30 minutes.

MicroCATs are instruments used to measure temperature, conductivity and pressure. These MicroCATs are attached to the tall moorings at target depths of 60, 475, 950, 1450, 2250 and 50 m above the bottom. The sample interval of the MicroCATs is 15 minutes. Additional Sea-Brid SBE56 thermistors are used for a more detailed temperature profile, therefore, improving the estimation of the thermocline. The thermistors are attached to the tall moorings at target depths of 180 and 725 m. The thermistors sample with a frequency of 5 minutes.

For M1 the instruments are attached at different target depths. The ADCP is at 300 m and is looking upward. The Nortek Aquadopp current meters are positioned at 700, 1200, 1430 and 1645 m. The MicroCATs are at 50, 100, 350, 500, 700, 900, 1200, 1430 and 1645 m. The sample interval of the ADCP differs to the sample rate of the IC moorings, and is set to 20 minutes [8].

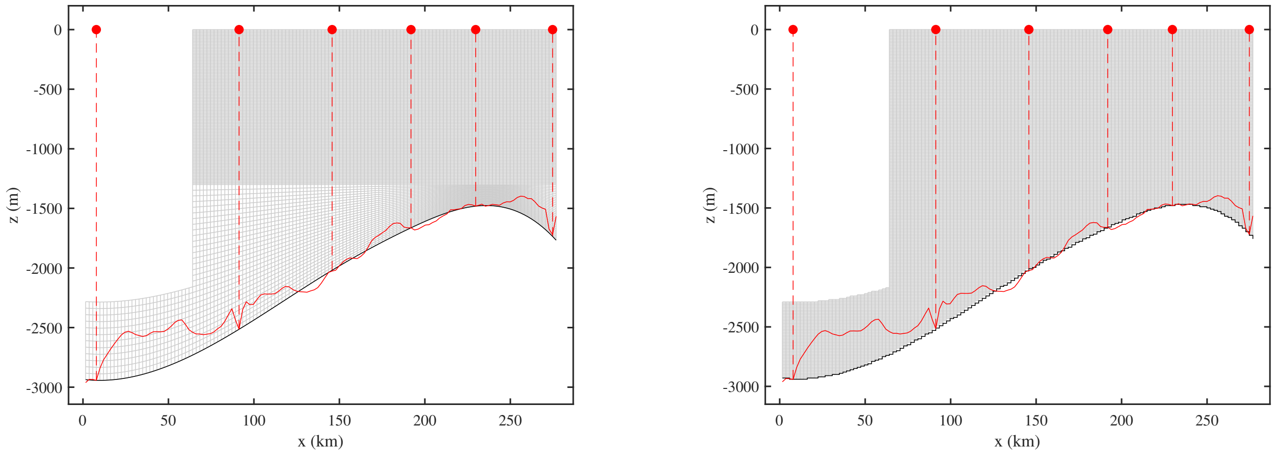

(a) *Original non-uniform grid*

(b) *Interpolated uniform grid*

Figure 3.5: *Bottom topography and interpolated grid. Horizontal axis and vertical axis are respectively the distance along the mooring array x and the height to the surface z. Red dotted lines are mooring lines, continues red line is the bottom topography and continues black line is the bottom topography of the used grid. (a) Original non-uniform grid (b) Interpolated uniform grid.*

3.3 Data processing

This section describes the performed data processing [8] of the mooring measurements, starting with the velocity. The velocity profiles are determined by combining the data of the ADCP, RCM11's and Aquadopps. The velocity profiles are filtered with a 41-hour low-pass Butterworth filter to remove the tides and inertial motions. There are a couple of instruments that malfunctioned, which resulted in data gaps. These data gaps are filled using vertical regression coefficients, as the velocity shows strong barotropic components [8].

The vertical velocity profiles per mooring are determined before horizontally interpolating the data to a two-dimensional grid. The data is interpolated to a grid which consists of two parts: an upper Cartesian grid and a lower non-Cartesian grid, as shown in fig. 3.5a. The upper grid ranges from the surface to a depth of 1300 m, and has horizontal and vertical spacings of respectively 2 km and 10 m. The lower grid is a bottom-following contour with a fixed horizontal spacing of 2 km. The vertical spacing depends on the bottom depth, and varies between the deep basin and top of the Reykjanes Ridge, respectively equal to 55 m and 15 m. The velocities are extrapolated to the surface using shape-preserving piecewise cubic Hermite interpolants. The velocities along U and across V the Reykjanes Ridge are determined by rotating the velocities clockwise with 10 deg. After the rotation the determined profiles are resampled to daily intervals.

A similar technique is used to calculate the temperature T and salinity S profiles. Here the T and S profiles are extended to the surface with the help of nearby Argo floats and by measurements of weekly sea surface temperatures.

The mooring data is finally interpolated to a fully Cartesian grid, as shown in fig. 3.5b. The top part of the original grid from fig. 3.5a remains the same; however, the bottom part is now also a Cartesian grid. The entire grid has the exact spacing of 2 km by 10 m. The fully Cartesian grid is preferred as the calculations of the first-surface and EOF-modes are more convenient, as each grid point covers the same area within the mooring cross-section.

Chapter 4

Results

Chapter Abstract

This chapter describes the results and corresponding discussion of the mooring data. The chapter starts with a general data exploration of the mooring array to show the main characteristics of the data. Further on, the mesoscale mixing is derived for each mooring separately on seasonally, weekly and daily basis. The mesoscale mixing on a weekly and daily basis resulted in strong intermittency. This intermittency effect is a new approach to how mesoscale mixing should be interpreted. The mesoscale mixing is determined with three different methods: using the velocity measured from the moorings, using first-surface modes derived from the stratification profiles of the moorings and using first-surface modes derived from the World Ocean Atlas data. The advantage of these first-surface modes is that it does not require velocity measurements from mooring data, as altimetry data could be used instead.

4.1 Data Exploration

This section gives a general overview of the mooring data. Figure 4.1 shows the average values of multiple parameters over the mooring cross-section. The average value is determined over the entire measuring period from 13/07/2014 up to and including 15/07/2018. The velocity across U and along V the Reykjanes ridge are respectively shown in figs. 4.1a and 4.1b. The velocity U is significantly smaller in magnitude compared to V, as the IC flows along the ridge. The velocity V shows two maxima near the surface at a distance x of roughly 85 km and 200 km. These two maxima represent the two cores of the current going in the north-eastward direction. These two cores are also found in previous studies [8, 17]. The flow does not vanish near the bottom; therefore, indicating the presence of bottom flows. Figure 4.1c shows the cross-section of the EKE. The value of the EKE in between the moorings is incorrect, as this interpolation of U and V between the moorings did not take into account the evolution of the EKE. Nevertheless, the value of EKE is correct along the moorings, where it shows a maximum near the surface and it decays rapidly towards zero.

The cross-section of the conservative-temperature T is shown in fig. 4.1d. The temperature shows a strong gradient for temperatures of 4.5 °C and higher. This gradient is also observed in the cross-section of the neutral density γ_n, as shown in fig. 4.1e. The origin of this gradient comes partially from the salinity S, as shown in fig. 4.1f. The cross-section of the salinity can be used to distinguish three different water masses, as shown in a previous study [17]. The salinity shows a minimum at a depth of 1 km between a distance of 100 to 190 km, which represents the Labrador Sea water (LSW). The salinity maximum above the top of the ridge is the warmer Subpolar Mode Water (SPMW). The salinity minimum below a depth of roughly 2 km is the colder overflow water from the Iceland-Scotland Ridge. The stratification N^2, defined as the buoyancy frequency of eq. (2.27) is shown in fig. 4.1g. The water is strongly stratified near the surface due to the relatively high temperature combined with low salinity. Below a depth of roughly 1 km the stratification remains roughly $2 \times 10^{-6}\,\mathrm{s}^{-1}$, therefore, this layer is considered more or less homogeneous.

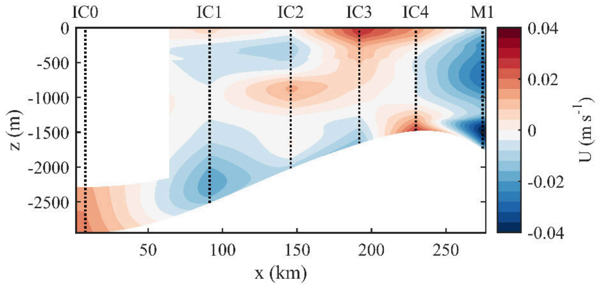

(a) *Velocity across ridge*

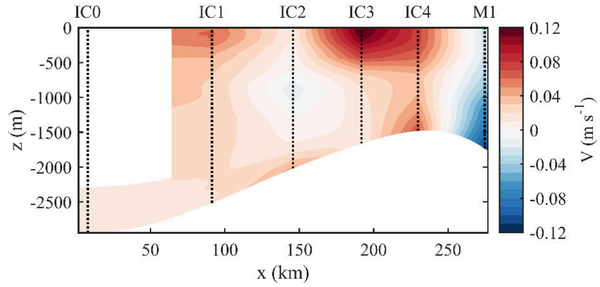

(b) *Velocity along ridge*

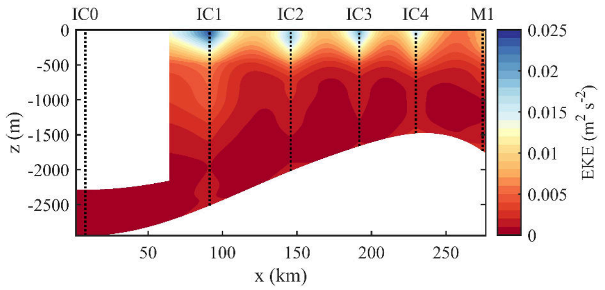

(c) *Eddy kinetic energy*

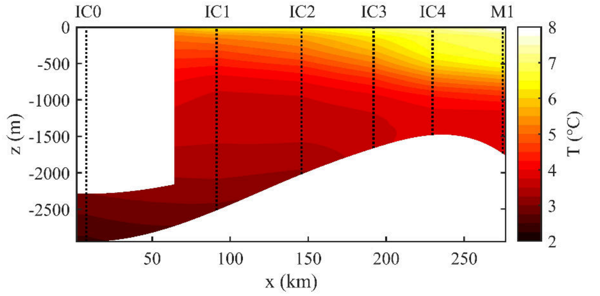

(d) *Conservative temperature*

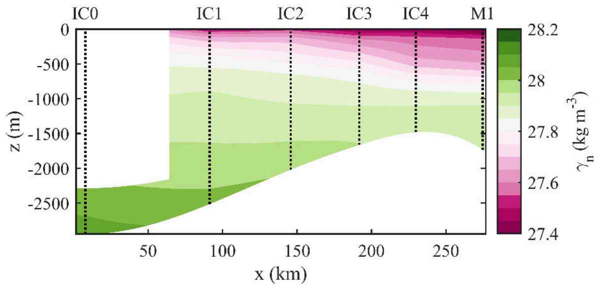

(e) *Neutral density*

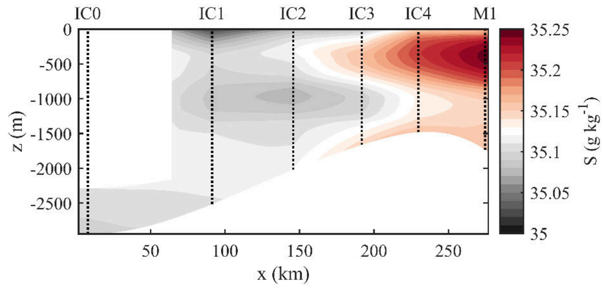

(f) *Absolute salinity S*

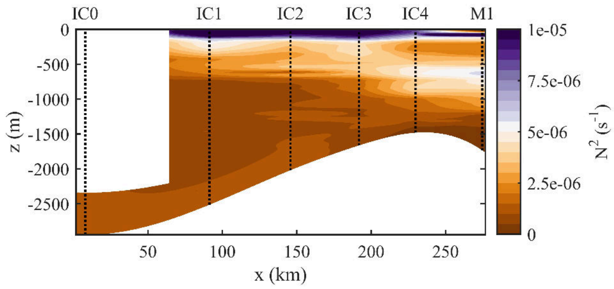

(g) *Buoyancy frequency*

Figure 4.1: *Average water properties of the mooring cross-section across the Irminger Current. The average is taken over the entire measuring period from 13/07/2014 up to and including 15/07/2018. Black dotted lines indicate the mooring lines. The moorings from west to east are IC0 up to IC4 and M1.*

4.2 Mixing on seasonally time scales

The MM is determined for the mooring IC3 on a seasonal basis. This mooring is positioned near the centre of the mooring array, and therefore it is easier to compare to the other moorings. Within this section, the MM is only analysed for the year 2017, as the mooring data during this year did not contain any data gaps.

Figure 4.2 shows the seasonally averaged parameters for IC3 in 2017. The seasons winter, spring, summer and autumn correspond to the months (J,F,M),(A,M,J),(J,A,S) and (O,N,D). U and V are respectively shown in figs. 4.2a and 4.2b. The magnitude of V is in general larger than U, similar to fig. 4.1. The maximum velocity for each season is observed near the surface, with the autumn having the highest maximum of all seasons. The mooring IC3 is positioned in the Eastern core of the IC; therefore, the core is relatively strong during the autumn and the spring. Figure 4.2c shows the root-mean-square velocity u_{rms}, which strongly reflects the behaviour of V.

Figure 4.2d shows the conservative temperature T for the different seasons. The surface temperature is highest during the summer and autumn, while the lowest surface temperature is observed during the winter. The salinity profiles are shown in fig. 4.2e, here the salinity appears to have a maximum at a depth of 500 m and minimum at 1000 m, these maximum and minimum respectively belong to the SPMW and LSW. During the summer and autumn, a relatively low salinity is observed, which is caused due to the strong stratification that keeps the low salinity water near the surface, while in winter the vertical mixing distributes the low salinity water over deeper layers. The profiles of the neutral density are visualised in fig. 4.2f, which show the strong stratification near the surface during the summer and autumn. This strong stratification is also seen in the N^2 profiles of fig. 4.2g and is caused by the relatively high T and low S near the surface. The stratification of fig. 4.2g is, however, not the actual stratification, as the profile shows local minima at the positions where S and T are measured. The deviating N^2 profiles originate from the vertical interpolation of the mooring data, which did not fully succeed in determining the stratification due to the low values of N^2. Nevertheless, the stratification profiles are accurate enough to be used within this study.

The MM is estimated for IC3 on a seasonal basis using the root-mean-square velocity u_{rms} as described in sections 2.1 to 2.3 and is shown in fig. 4.3. The eddy deformation radius L_d is estimated using the first-surface modes of section 2.4. This radius L_d during the winter, spring, summer and autumn is respectively equal to 10.4, 10.2, 11.0 and 11.3 km. These magnitudes of L_d match with previous studies [19,33], which estimate L_d between 10 to 20 km at the IS. The mixing efficiency Γ and eddy decorrelation timescale γ^{-1} are both assumed to be constant and equal to respectively 0.35 and $1.66\,\mathrm{d}^{-1}$ [19]. The non-suppressed mixing K_{MLT} is shown in fig. 4.3a. The value of K_{MLT} depends on both u_{rms} and L_d, however, the variation in u_{rms} is lager than the variation in L_d, therefore, the profile of K_{MLT} shows a strong correlation with u_{rms}.

The suppression factor $S_\perp$ of fig. 4.3b is derived with eq. (2.22), using δu of eq. (2.25). The suppression factor $S_\perp$ uses the velocities U and V in respectively north and eastward direction instead of the velocities along and across the Reykjanes Ridge. The suppression is strong for values of $S_\perp$ close to 0, while the suppression is weak for values of $S_\perp$ close to 1. The water column is especially suppressed near the surface due to a large velocity difference in δu, meaning that the velocity of the current $\mathbf{U}$ strongly deviates from the Doppler-shifted Rossby wave speed $\mathbf{c_w}$. $S_\perp$ shows multiple maxima, which indicate areas of low suppression where δu is close to zero, therefore, $\mathbf{c_w} \cdot \mathbf{e_U}$ is approximately equal to $||\mathbf{U}||$. At these maxima the suppressed mixing $K_\perp$ roughly equals the unsuppressed mixing K_{MLT}.

The suppressed cross-current mixing $K_\perp$ is shown in fig. 4.3c. There is a significant difference between $K_\perp$ and K_{MLT} due to the suppression factor. For K_{MLT} the strongest mixing is estimated during the autumn, while, for $K_\perp$, the autumn is strongly suppressed near the surface and the strongest mixing is estimated during the winter. Due to the suppression, the mixing $K_\perp$ is on average 29.7 % of the magnitude of the non-suppressed mixing K_{MLT}, which is a stronger suppression compared to previous studies [19]. This difference in suppression strength might be caused by two reasons: first, the MM is derived on shorter timescales, and second, the suppression factor is approached as a two-dimensional mechanism instead of a one-dimensional mechanism. Further on, figs. 4.3a and 4.3c show that the MM is definitely not constant in time, as it is strongly varying throughout the seasons.

Figure 4.4 shows the mixing properties of IC3 for the entire measuring period from 13/07/2014 up to and

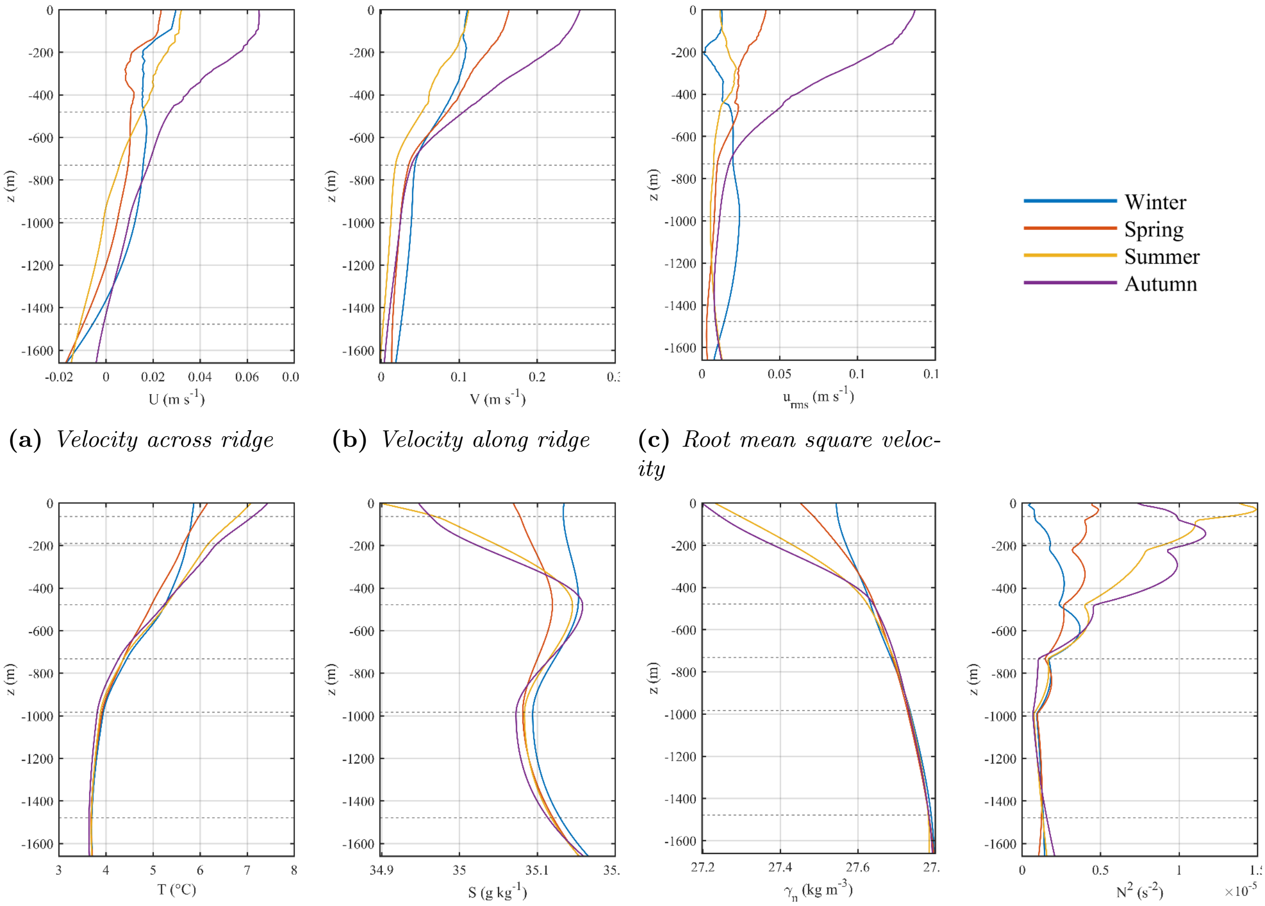

(a) *Velocity across ridge* **(b)** *Velocity along ridge* **(c)** *Root mean square velocity*

(d) *Temperature* **(e)** *Salinity* **(f)** *Neutral density* **(g)** *Stratification*

Figure 4.2: *Seasonal averaged water properties for IC3 during the year 2017. The seasonal properties are plotted as function of depth. Each season is presented with a different color: winter (blue), spring (red), yellow (summer), purple (autumn)*

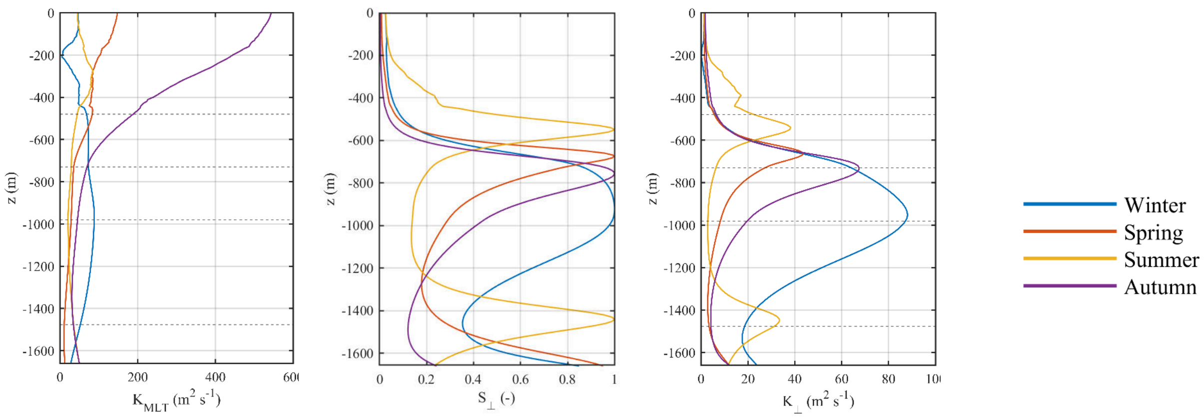

(a) *Non-suppressed mixing* **(b)** *Suppression factor* **(c)** *Suppressed cross-current mixing*

Figure 4.3: *Similar to fig. 4.2, showing the seasonal mixing properties.*

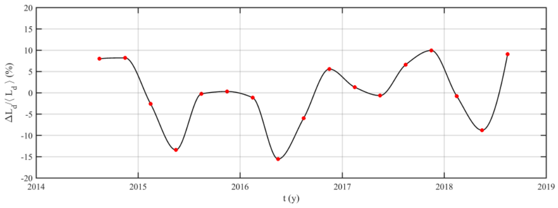

(a) *Deformation radius*

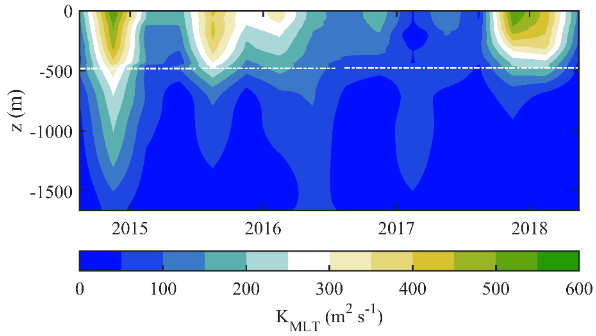

(b) *Non-suppressed mixing*

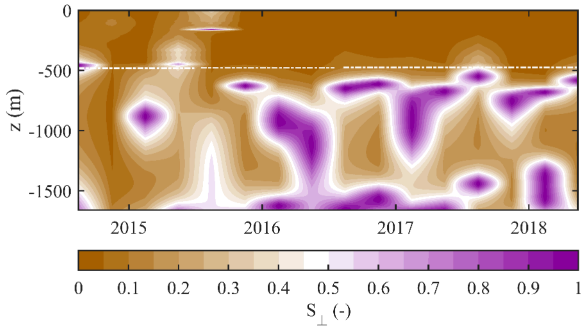

(c) *Suppression factor*

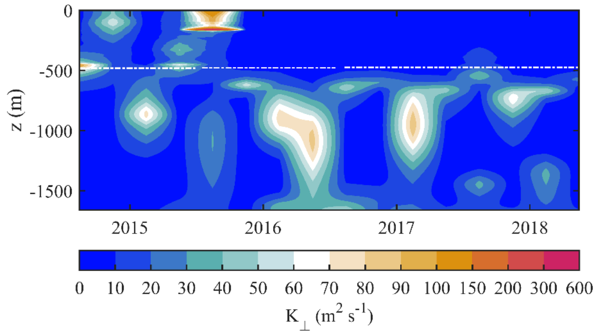

(d) *Suppressed cross-current mixing*

Figure 4.4: *Seasonal mixing determined for IC3 during the full measurement period from 13/07/2014 up to and including 15/07/2018. (a) The difference of the deformation radius to its average value as a function over time. Red dots indicate the deformation radius per season. The black dotted line is the spline interpolation using the red dots. The average deformation radius of IC3 on a seasonal basis equals 10.3 km. (b),(c) and (d) respectively indicate the mixing without suppression, the suppression factor and the suppressed cross-current mixing.*

including 15/07/2018. Figure 4.4a shows the deformation radius as function of time, with an average deformation radius $\langle L_d \rangle$ of 10.3 km. L_d shows a clear variation over time: during the spring L_d is smallest, while the autumn and winter show the highest L_d. The maximum deviation of $\langle L_d \rangle$ is observed during the spring of 2016, with a deviation of $-15.6\,\%$. L_d shows a strong yearly variation; therefore, L_d can not be assumed to be constant.

Figure 4.4b shows K_{MLT} as function of both time and depth for IC3. Within this figure, the white dotted line indicates the position of the ADCP, above this line the velocity measurements are performed by the ADCP, while below the line the velocity is determined by interpolation of the single-point measurements. The mixing K_{MLT} shows a slight deviation between these areas, which might be caused due to the difference in measurement instruments and data processing. Further on, K_{MLT} shows strong non-suppressed mixing near the surface during the autumn and winter.

Figure 4.4c shows $S_\perp$ as a function of time and depth for IC3. The suppression remains strong near the surface, however, the suppression weakens below the depth of the ADCP. The suppression $S_\perp$ appears to be time-dependent without a clear seasonal cycle. The evolution of $K_\perp$ as a function of time and depth for IC3 is shown in fig. 4.4d. Near the surface the mixing is strongly suppressed, however, during the autumn of 2014 and summer of 2015, there remains some suppressed mixing. The strongest mixing is in general estimated during the winters, which compares with the results of fig. 4.3c.

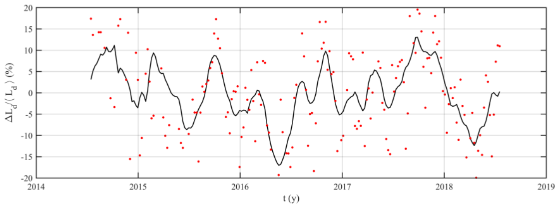

(a) *Deformation radius*

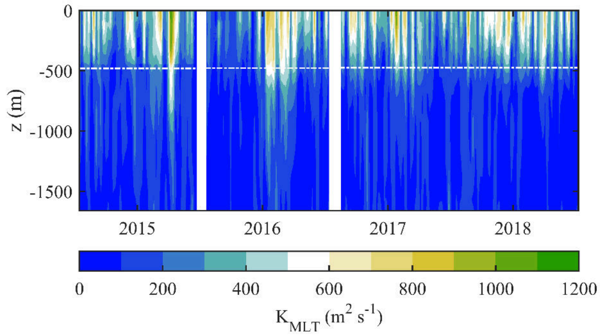

(b) *Non-suppressed mixing*

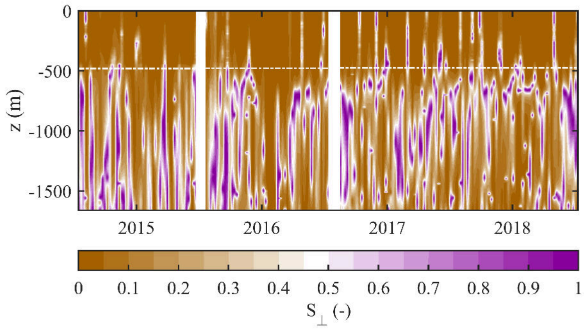

(c) *Suppression factor*

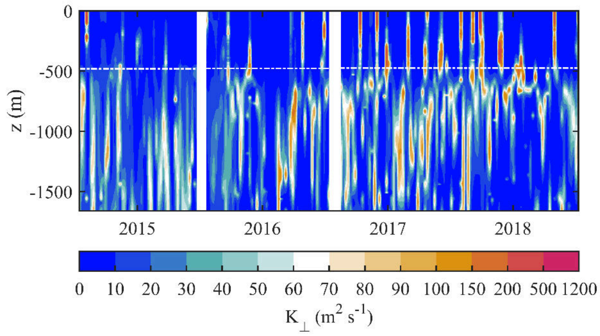

(d) *Suppressed cross-current mixing*

Figure 4.5: *Similar to fig. 4.4, but on a weekly basis. (a) Black dotted line is the running average over the deformation radius. The width of the running average is* 60 *days. The average deformation radius of IC3 on a weekly basis equals 10.3 km. (b),(c) and (d) show two white gaps, which are the data gaps due to servicing of the moorings.*

4.3 Mixing on weekly time scales

This section discusses the results of MM on a weekly basis. An overview of the weekly MM for IC3 is shown in fig. 4.5. The deformation radius L_d is shown in fig. 4.5a, where L_d shows large variations similar to the seasonal averaged data of section 4.2. However, the yearly cycle of L_d is less clear compared to the seasonally averaged L_d. On the weekly basis L_d equals on average 10.3 km. L_d contains noisy data as seen from the variations in fig. 4.5a, this noise is filtered out by using a 60 days running average. The maximum deviation of L_d from its average is observed during the spring of 2016, with a deviation of $-17\,\%$.

Figure 4.5b shows the non-suppressed mixing K_{MLT} for IC3. Near the surface, the mixing is appearing in bursts, a short period of mixing is followed by a period of lower to none mixing. These bursts are referred to as intermittent behaviour. This derived intermittency of K_{MLT} is a new approach to MM, as it shows the time dependency of MM on short time scales. Further on, K_{MLT} shows that strong mixing near the surface correlates to deeper penetration of the mixing. However, there is again a clear difference between K_{MLT} in the region above and below the ADCP.

Figure 4.5c shows the suppression factor $S_\perp$ for IC3. The average $S_\perp$ equals 0.242, therefore strongly suppressing $K_\perp$. $S_\perp$ shows strong intermittency, which is especially caused due to the variability of δu. The intermittency of K_{MLT} and $S_\perp$ is also observed in $K_\perp$, as shown in fig. 4.5d. Further on, the profile of $K_\perp$ remains influenced by the ADCP depth. Here, $K_\perp$ below the ADCP does show smoother transitions between periods of mixing.

The MM on a weekly basis is derived for each mooring separately, as shown in appendix A. Figure A.1 shows the deformation radius L_d for each mooring as function of time. The average L_d ranges from 10.3 km to 12.3 km, respectively of IC3 and IC1. All the moorings show a deformation radius L_d which varies over time. The value of L_d depends on the stratification, as L_d is determined using first-surface modes. Therefore, the small variations of IC1 and IC2 might be caused due to the relatively lower stratified profiles, as shown in fig. 4.1g. The moorings IC4 and M1 show a clear seasonal cycle, which might be caused due to the stronger stratified SPMW. This clear seasonal cycle is a novel result of this study, as such a seasonal cycle has not been found in previous studies at the IS [17].

Figure A.2 shows the evolution of K_{MLT} for each mooring separately, with all moorings showing a similar intermittency behaviour. The non-suppressed mixing K_{MLT} is mostly strongest near the surface and goes gradually to 0 near the bottom for IC1, IC2 and IC3. However, for IC4 and especially for M1 the value of K_{MLT} often increases near the bottom. The increase of K_{MLT} might be caused due to the strong velocities near the bottom, as shown in figs. 4.1a and 4.1b. These strong velocities near the bottom could be explained by topographic waves [33]. The non-suppressed mixing K_{MLT} appears to be in general the strongest near the surface for all moorings. It also appears to be that stronger at the surface is more likely to penetrate greater depths. Overall, IC1 observes the most mixing near the surface, which could be caused due to the high EKE below the surface, as shown in fig. 4.1c.

Figure A.3 shows $S_\perp$ for each mooring separately, here $S_\perp$ remains to show strong intermittency for all moorings. Regions of weak suppression occur at different depths, for example, at IC1, the region of weak suppression is between 1500 and 2500 m, while for M1 this region is between 800 and 1200 m. Figure A.4 shows $K_\perp$ for each mooring, here $K_\perp$ remains to show the strong intermittency without a clear seasonal cycle.

4.4 Mixing on daily time scales

This section analyses the MM on a daily basis for IC3. Figure 4.6a shows the deformation radius L_d for both the daily and weekly-based mixing. The 60 day running average of both daily and weekly L_d do overlap, except for the offset during the beginning of the deployment.

Figures 4.6b and 4.6d show K_{MLT} on respectively a weekly and daily basis for the period from 01/06/2017 up to and including 31/12/2017. This period is shorter compared to the previously used periods of sections 4.2 and 4.3, as the fine resolution of the daily mixing is better visualized using shorter periods. This particular period is chosen as it gives a good representation of the entire measuring period. The K_{MLT} on a daily basis overlaps with the regions of stronger mixing on a weekly basis. The intermittency effect is present on both time scales; therefore, we can conclude that the intermittency takes place in the order of days to weeks. The mixing based on the daily data appears to have more noise, which might be caused due to the occurring instabilities in the stratification on a daily basis. For this study, the MM is rather approached on a weekly basis, as on a weekly basis there is less noise compared to the daily based mixing.

Figures 4.6c and 4.6e show $K_\perp$ respectively on a weekly and daily basis for the period from 01/06/2017 up to and including 31/12/2017. Similar to K_{MLT} the weekly and daily $K_\perp$ overlap, however, the daily $K_\perp$ shows again more noise. Further on, both the weekly and daily K_{MLT} and $K_\perp$ show a clear intermittency pattern.

The second research question RQ2 of section 1.4 can now be answered, as the characteristics of a MM time series of a single water column are described as following: on a timescale of seasons the MM shows a yearly cycle, with the strongest effective mixing occurring in the winter. On shorter timescales, in the order of weeks to days, the MM occurs in bursts: periods of intense mixing followed by periods of rests. The strongest unsuppressed mixing occurs at the surface, with the strength of the mixing related to the penetration depth of the mixing itself.

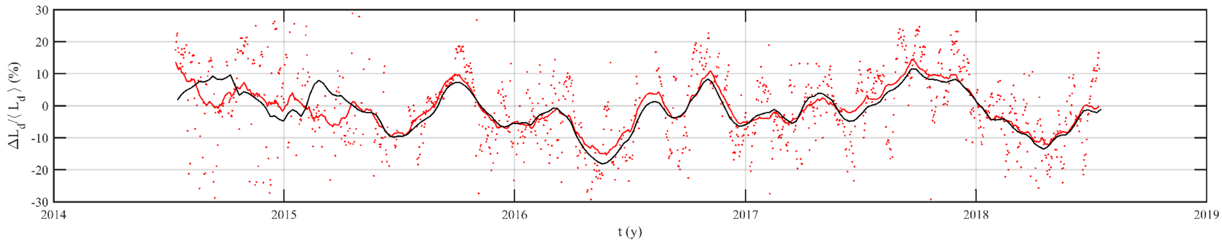

(a) *Deformation radius*

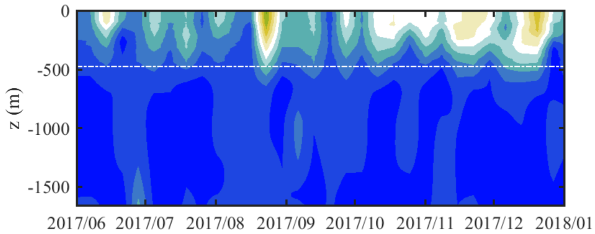

(b) *Weekly non-suppressed mixing*

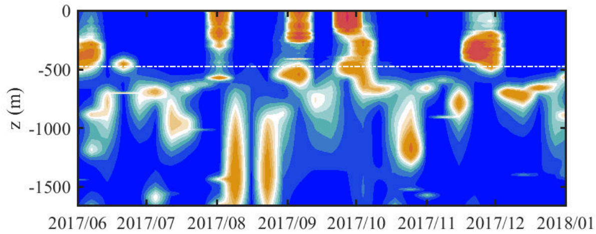

(c) *Weekly suppressed cross-current mixing*

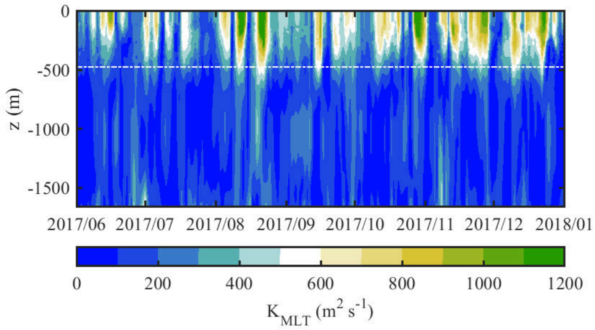

(d) *Daily non-suppressed mixing*

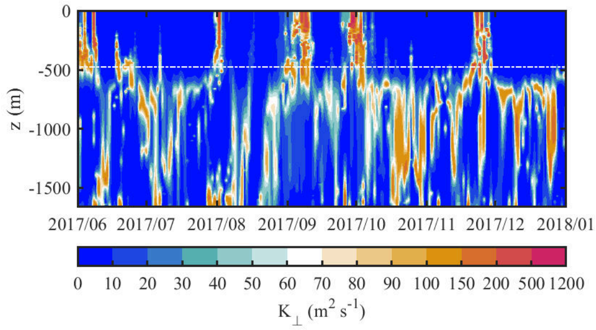

(e) *Daily suppressed cross-current mixing*

Figure 4.6: *Weekly and daily mixing for IC3. (a) Difference of the deformation radius to its average value as a function of time. The average deformation radius of IC3 on a weekly (black) and daily (red) basis are respectively equal to 10.3 km and 10.2 km. The deformation radius is determined for the full measurement period from 13/07/2014 up to and including 15/07/2018. The continuous lines are the running averages over the deformation radii with a width of* 60 *days. The red dotted points are the deformation radii based on daily averages. (b,d) and (c,e) respectively indicate the non-suppressed mixing and the suppressed cross-current mixing during the period from 01/06/2017 up to and including 31/12/2017. (b,c) and (d,e) are respectively weekly and daily based.*

4.5 Alternative methods in determining mesoscale mixing

This section describes the results of two alternative methods to determine the MM. Both methods rely on first-surface modes, as described in section 2.4. One method uses first-surface modes derived from the stratification profiles of the moorings, while the other method uses first-surface modes derived from the stratification profiles of the WOA [19].

The first alternative method to be discussed is the method that uses the first-surface modes derived from the stratification profiles of the moorings. Before estimating the MM the correct bottom boundary condition of ϕ needs to be determined. The bottom boundary condition is either rough or flat, as described in section 2.4. The correctness of these boundary conditions is verified using the first EOF mode of current meters. Within this study, the first three EOF modes of U, V and u_{rms} are all considered, as shown in fig. 4.7a. The first EOF modes, EOF1, all clearly overlap. However, the second and third EOF modes start to deviate from each other around a depth of 300 m. Only the first EOF mode is required to verify the boundary conditions of ϕ , as this is the gravest EOF which should resemble the gravest surface mode [31]. Concerning the first EOF mode, one could use the EOF mode of U,V or u_{rms}, which all overlap for EOF1. Often the EOFs of U and V are used to estimate the vertical structure of ocean eddies [37], however, as the mesoscale mixing is defined as a function of u_{rms}, we prefer to use the EOF1 of u_{rms}. This EOF1 u_{rms} is a monopole gradually decaying to 0 at the bottom and explains a variance of 77.9%, while EOF2 and EOF3 respectively explain a variance of 11.9% and 4.9%. The variation of EOF1 u_{rms} over time is shown in fig. 4.7c, showing a significant yearly variation.

The EOF1 u_{rms} can now be compared to the vertical structure ϕ. Figure 4.7b shows the ϕ estimated using flat and rough boundary conditions for both the WKB and RK4 solution methods. The estimated vertical structures significantly overlap with the results of previous studies [33]. ϕ estimated with the flat bottom condition does not overlap with the profile of EOF1 u_{rms}, especially not near the bottom. However, ϕ estimated with the rough bottom condition overlaps slightly with the profile of EOF1 u_{rms}, as both structures result in a monopole gradually decaying to 0. The rough bottom modes appear to be less surface intensified compared to the EOF1 u_{rms}. Overall, the modes from the rough bottom condition, which are the first-surface modes, suit best for the moorings. These rough bottom first-surface modes will therefore be used to estimate the vertical structure ϕ.

Further on, there needs to be decided which solution method for ϕ suits best. Figure 4.7b shows that both WKB and RK4 solution methods overlap for the rough bottom condition. Still, the RK4 is preferred due to its improved ability to solve for the complex stratification profiles numerically. In contrast, the WKB solution method might result in more noise [33]. The vertical structure ϕ derived from the first-surface modes using the RK4 solution method is similar to the surface modes as found in literature [19].

The vertical structure ϕ is utilised to estimate the MM on a weekly basis for IC3, as shown in fig. 4.8a. ϕ is normalised to 1 at the surface and gradually drops down to 0 at the bottom. The value of ϕ vanishes near the bottom, as these first-surface modes do not include topographic waves [33]. Further on, ϕ shows deep penetration during the winters, especially during the year 2015.

Figure 4.8b shows K_{MLT} derived using the first-surface modes based on the stratification as measured by the moorings. K_{MLT} remains to show intermittency and deeper penetration during periods of strong mixing near the surface. The K_{MLT} based on the first-surface modes shows significant overlap with the K_{MLT} based on the velocity measurements of fig. 4.5b. However, there are two main differences between the first-surface and velocity approaches: firstly, the K_{MLT} based on the first-surface modes decays always to zero at the bottom. Secondly, the K_{MLT} based on the first-surface modes does not show a clear transition near the ADCP in the vertical profile.

Figure 4.8c shows $K_\perp$ derived with the first-surface modes in combination with $S_\perp$ of fig. 4.5c. The $K_\perp$ from the first-surface modes overlaps with the $K_\perp$ based on the velocity measurements of fig. 4.5d. However, $K_\perp$ derived from the first-surface modes shows higher local maxima due to the deeper penetration of ϕ.

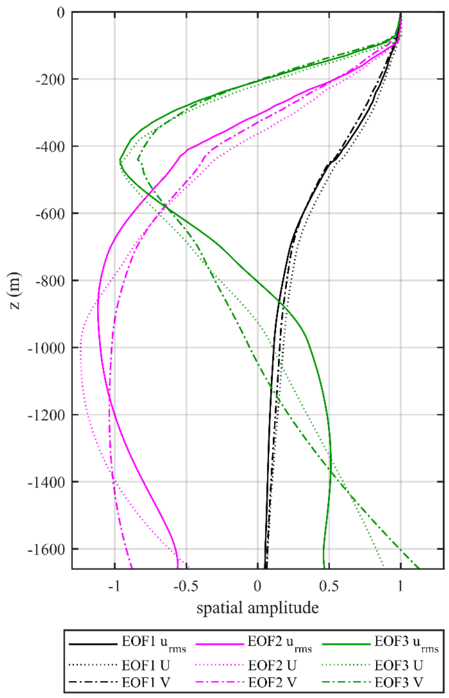

(a) *First three EOF modes for u_{rms}, U and V.*

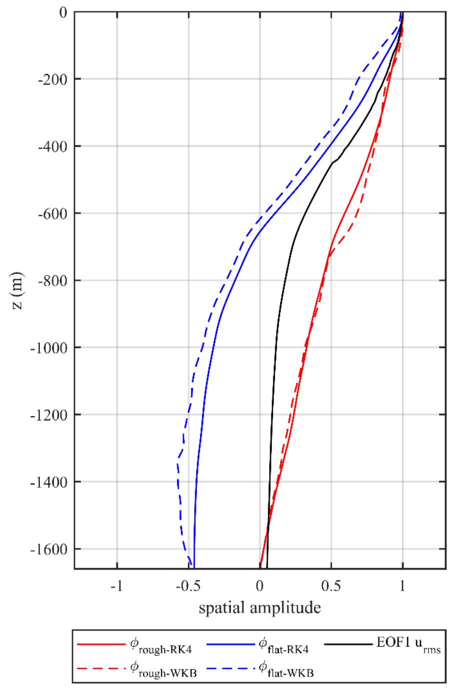

(b) *FS modes with different boundary conditions and solution methods, compared to EOF1 u_{rms}.*

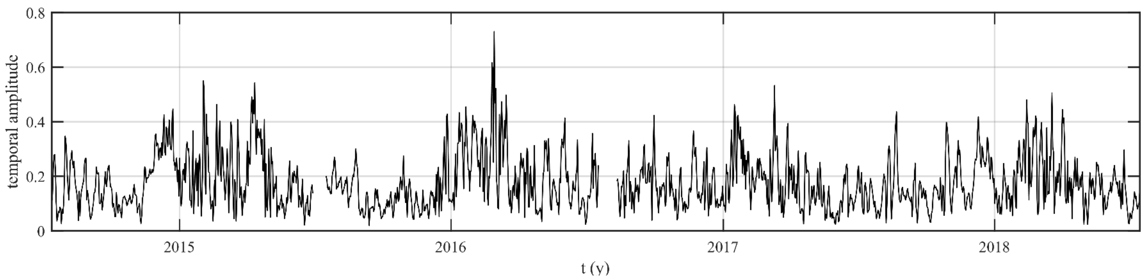

(c) *Temporal amplitude EOF1 u_{rms}.*

Figure 4.7: *Validation of first-surface boundary condition and solution method. (a) first three EOF modes for u_{rms}, U and V. (b) comparison of vertical modes with EOF1 u_{rms} (c) temporal amplitude of EOF1 u_{rms}.*

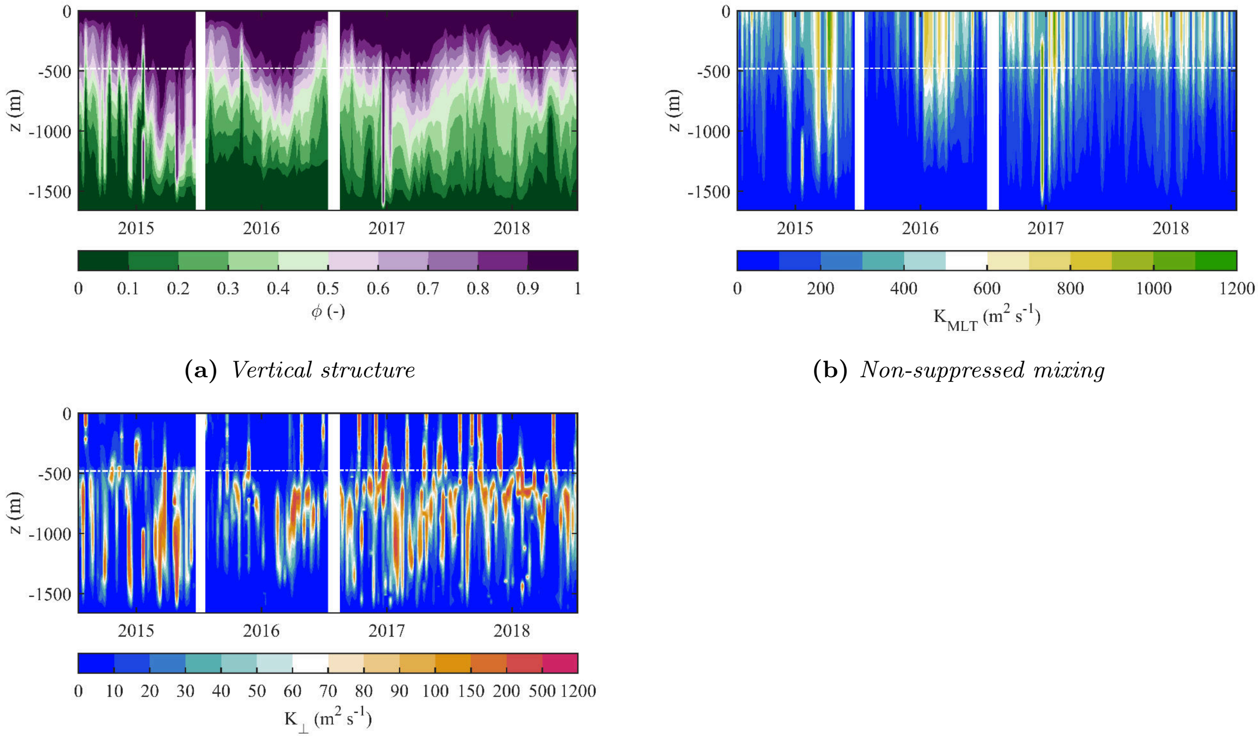

(a) *Vertical structure*

(b) *Non-suppressed mixing*

(c) *Suppressed cross-current mixing*

Figure 4.8: *Weekly mixing for IC3 based on first-surface modes for the period from 13/07/2014 up to and including 31/12/2017.*

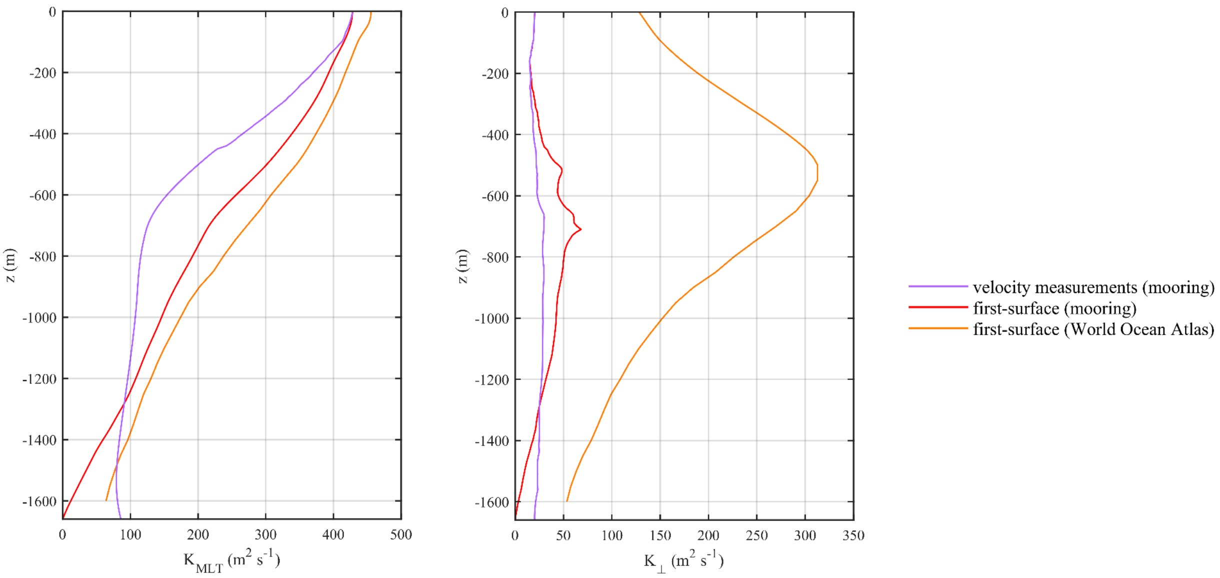

(a) *Vertical structure* **(b)** *Suppressed cross-current mixing*

Figure 4.9: *Comparison of average mesoscale mixing profile of IC3 based on velocity measurements (purple), first-surface modes (red) and World Ocean Atlas-data (orange) [19]. The mixing estimated from the moorings uses weekly averaged data and the WOA estimated mixing uses yearly averaged data.*

Figure 4.9 shows a comparison between the different strategies to determine MM. Within this figure, there are three strategies compared: velocity measurements from moorings, first-surface modes using the stratification from moorings and first-surface modes using the stratification from the WOA. The first-surface modes from the WOA are determined in a previous study [19] and are interpolated to the position of IC3. Figure 4.9a shows the resulting K_{MLT}, with all three strategies in the same order of magnitude. The original method of using the velocity measurements deviates from the other methods, as the K_{MLT} of this method does not approach 0, which might be caused due to the presence of topographic waves [19, 38]. Further on, K_{MLT} estimated from the velocity measurements deviates also around halve depth, the origin of this offset remains yet unclear but might be related to the difference in the gradient of the EKE compared to the gradient of the stratification N^2.

Figure 4.9b shows $K_\perp$ for the different strategies. The strategy using the WOA data shows a large offset, which might be caused due to three different reasons: first, the offset can be caused due to a different approach of the suppression factor, as the study of the WOA uses an alternation of one-dimensional suppression instead of the two-dimensional suppression as derived in section 2.3. Second, the study of the WOA uses annual based data instead of weekly based data. And third, the suppression factor of the study from the WOA uses velocities determined by thermal wind instead of mooring measurements. Further on, the method using velocity measurements shows a relatively increased offset for $K_\perp$ compared to using first-surface modes from moorings. This offset appears to occur not only at IC3, but for all the moorings.

The third research question RQ3 of section 1.4 can now be answered. This research question addresses the comparison in mixing derived from first-surface modes and velocity measurements. We have seen that for both methods the unsuppressed mixing is in the same order of magnitude; however, there is an offset near the bottom and around half depth. These two offsets might be caused due to a difference in the gradient of the EKE and stratification, and due to the lack of topographic waves in first-surface modes. The relative magnitudes of these offsets increase when suppression is included. The first-surface modes can therefore be used to roughly estimate the unsuppressed mixing, however, not yet the suppressed mixing.

Chapter 5

Conclusion and Outlook

This study aims to improve the understanding of mesoscale mixing (MM) time series estimated from moorings. This MM is a combination of Mixing Length Theory, suppression theory and vertical modes. Within this study the MM is derived from the velocity measurements of moorings deployed across the Irminger Current in the Irminger Sea. The moorings provide a high temporal resolution and are therefore suitable to determine the MM on short timescales up to days. On a timescale of seasons, the MM shows a significant variation throughout the year, with the strongest effective mixing occurring in the winter. However, on shorter timescales, in the order of weeks to days, the MM shows clear intermittency. This intermittency means a series of strong mixing bursts followed by periods of hardly any mixing. The proven intermittency has previously not been documented and is a novel insight gained through this project. Further on, the strongest unsuppressed mixing occurs at the surface, with the strength of the mixing related to the penetration depth of the mixing itself.

The strength of the MM depends also on the deformation radius, which represents the length scale over which a fluid parcel conserves its properties before mixing with its surrounding fluid. This deformation radius is proven to be a function of time, with variations up to 20 %. The average deformation radius differs per mooring and ranges from 10.3 km to 12.3 km. The moorings positioned on the eastern side in the Subpolar Mode Water show a clear seasonal cycle of the deformation radius, which might be caused due to locally stratified water. In general, the deformation radius reaches its maximum during the autumn, which induces stronger unsuppressed mixing.

Further on, the MM is derived with alternative methods using first-surface modes. First-surface modes do not take into account topographic waves; therefore, resulting in an underestimation of the MM near the bottom. The first-surface modes show an additional offset at half depth compared to the MM derived from velocity measurements, which might be caused due to the strong gradient of the velocity near the surface compared to the gradient of the stratification. It turns out that the first-surface modes can be used to roughly estimate the unsuppressed mixing, however, not yet the suppressed mixing.

The conducted study tries to push the general understanding of MM a step forward. This study can be extended by multiple challenges and strategies. One of these strategies would be to extend the analysis to different moorings. This study focusses on five moorings within the Irminger Sea, which could be extended to any other full depth moorings with a high temporal resolution, to improve the understanding of MM globally. Another strategy would be to extend the approach of first-surface modes with topographic waves. When both first-surface modes and topographic waves are combined, the mixing over the entire water column could be estimated without the use of velocity measurements. It would be interesting to see how the MM based on velocity measurements compares with the MM derived from first-surface modes and topographic waves. Lastly, another strategy would be an advanced time-series analysis of MM to determine the direct triggers of the occurring bursts of mixing. All of these strategies contribute to the general understanding of MM, improving the implementation of eddy-resolving ocean simulations, therefore, contributing to the knowledge of ocean climates.

MM remains an open research topic. The first steps are made, yet, there are many steps to follow.

Bibliography

[1] Intergovernmental Panel on Climate Change. *Summary for Policymakers*, page 1–30. Cambridge University Press, 2014.

[2] Martha W. Buckley and John Marshall. Observations, inferences, and mechanisms of the Atlantic Meridional Overturning Circulation: A review. *Reviews of Geophysics*, 54(1):5–63, 2016.

[3] J. Lazier, Ross Hendry, Allyn Clarke, Igor Yashayaev, and Peter Rhines. Convection and restratification in the Labrador Sea, 1990-2000. *Deep Sea Research Part I: Oceanographic Research Papers*, 49, 10 2002.

[4] Sijia Zou, M Susan Lozier, and Martha Buckley. How is meridional coherence maintained in the lower limb of the Atlantic Meridional Overturning Circulation? *Geophysical Research Letters*, 46(1):244–252, 2019.

[5] Stefan Rahmstorf, Jason E Box, Georg Feulner, Michael E Mann, Alexander Robinson, Scott Rutherford, and Erik J Schaffernicht. Exceptional twentieth-century slowdown in Atlantic Ocean Overturning Circulation. *Nature climate change*, 5(5):475–480, 2015.

[6] Monika Rhein, Dagmar Kieke, Sabine Hüttl-Kabus, Achim Roessler, Christian Mertens, Robert Meissner, Birgit Klein, Claus W Böning, and Igor Yashayaev. Deep water formation, the subpolar gyre, and the meridional overturning circulation in the subpolar North Atlantic. *Deep Sea Research Part II: Topical Studies in Oceanography*, 58(17-18):1819–1832, 2011.

[7] T. Rossby. The North Atlantic Current and surrounding waters: At the crossroads. *Reviews of Geophysics*, 34(4):463–481, 1996.

[8] M. Femke de Jong, L. de Steur, N. Fried, R. Bol, and S. Kritsotalakis. Year-round measurements of the Irminger Current: variability of a two-core current system observed in 2014-2016. 2020.

[9] Maria K. Flatau, Lynne Talley, and Pearn P. Niiler. The North Atlantic Oscillation, surface current velocities, and SST changes in the subpolar North Atlantic. *Journal of Climate*, 16(14):2355–2369, 07 2003.

[10] Jerome Cuny, Peter B. Rhines, Pearn P. Niiler, and Sheldon Bacon. Labrador Sea boundary currents and the fate of the Irminger Sea water. *Journal of Physical Oceanography*, 32(2):627–647, 02 2002.

[11] Nathalie Daniault, Herlé Mercier, Pascale Lherminier, Artem Sarafanov, Anastasia Falina, Patricia Zunino, Fiz Pérez, Aida Ríos, Bruno Ferron, Thierry Huck, Virginie Thierry, and Sergey Gladyshev. The northern North Atlantic Ocean mean circulation in the early 21st century. *Progress in Oceanography*, 146, 07 2016.

[12] M. Susan Lozier, Sheldon Bacon, Amy S. Bower, Stuart A. Cunningham, M. Femke de Jong, Laura de Steur, Brad deYoung, Jürgen Fischer, Stefan F. Gary, Blair J. W. Greenan, Patrick Heimbach, Naomi P. Holliday, Loïc Houpert, Mark E. Inall, William E. Johns, Helen L. Johnson, Johannes Karstensen, Feili Li, Xiaopei Lin, Neill Mackay, David P. Marshall, Herlé Mercier, Paul G. Myers,

Robert S. Pickart, Helen R. Pillar, Fiammetta Straneo, Virginie Thierry, Robert A. Weller, Richard G. Williams, Chris Wilson, Jiayan Yang, Jian Zhao, and Jan D. Zika. Overturning in the Subpolar North Atlantic Program: A new international ocean observing system. *Bulletin of the American Meteorological Society*, 98(4):737–752, 04 2017.

[13] Kjetil Våge, Robert S Pickart, Artem Sarafanov, Øyvind Knutsen, Herlé Mercier, Pascale Lherminier, Hendrik M Van Aken, Jens Meincke, Detlef Quadfasel, and Sheldon Bacon. The Irminger Gyre: Circulation, convection, and interannual variability. *Deep Sea Research Part I: Oceanographic Research Papers*, 58(5):590–614, 2011.

[14] Michael S McCartney and Lynne D Talley. The subpolar mode water of the North Atlantic Ocean. *Journal of Physical Oceanography*, 12(11):1169–1188, 1982.

[15] Elena Brambilla, Lynne D Talley, and Paul E Robbins. Subpolar Mode Water in the northeastern Atlantic: 2. Origin and transformation. *Journal of Geophysical Research: Oceans*, 113(C4), 2008.

[16] HM Van Aken and G Becker. Hydrography and through-flow in the north-eastern North Atlantic Ocean: the NANSEN project. *Progress in Oceanography*, 38(4):297–346, 1996.

[17] N. Fried and M. Femke de Jong. Transport variability of the Irminger Current: Results from four years of mooring deployment between 2014 - 2018. In progress.

[18] Corinne B Trott, Bulusu Subrahmanyam, and Ebenezer S Nyadjro. Influence of mesoscale features on mixed layer dynamics in the Arabian Sea. *Journal of Geophysical Research: Oceans*, 124(5):3361–3377, 2019.

[19] Sjoerd Groeskamp, Joseph H. LaCasce, Trevor J. McDougall, and Marine Rogé. Full-depth global estimates of ocean mesoscale eddy mixing from observations. In progress, 2020.

[20] Julius J. M. Busecke and Ryan P. Abernathey. Ocean mesoscale mixing linked to climate variability. *Science Advances*, 5(1), 2019.

[21] Laura Jackson, Ron Kahana, T. Graham, Mark Ringer, T. Woollings, J.V. Mecking, and R.A. Wood. Global and European climate impacts of a slowdown of the AMOC in a high resolution GCM. *Climate Dynamics*, 45:1–18, 03 2015.

[22] Raffaele Ferrari and Maxim Nikurashin. Suppression of eddy diffusivity across jets in the Southern Ocean. *Journal of Physical Oceanography*, 40(7):1501–1519, 07 2010.

[23] Andreas Klocker and Ryan Abernathey. Global patterns of mesoscale eddy properties and diffusivities. *Journal of Physical Oceanography*, 44(3):1030–1046, 03 2014.

[24] L Prandtl. Report on the investigation of developed turbulence. National advisory committee for aeronautics technical memorandum 1231 (1949), translation of "Bericht uber Untersuchungen zur ausgebildeten Turbulenz.". *Zeitschrift fur angewandte Mathematik und Mechanik*, 5(2), 1925.

[25] Geoffrey Ingram Taylor. I. eddy motion in the atmosphere. *Philosophical transactions of the Royal Society of London. Series A, Containing papers of a mathematical or physical character*, 215(523-537):1–26, 1915.

[26] P Bradshaw. Possible origin of Prandt's mixing-length theory. *Nature*, 249(5453):135–136, 1974.

[27] Paulo S Polito and Olga T Sato. Do eddies ride on Rossby waves? *Journal of Geophysical Research: Oceans*, 120(8):5417–5435, 2015.

[28] Andreas Klocker, Raffaele Ferrari, and Joseph H. LaCasce. Estimating suppression of eddy mixing by mean flows. *Journal of Physical Oceanography*, 42(9):1566–1576, 04 2012.

[29] P.W.M. Jacobs and Z.A. Rycerz. 4 - molecular dynamics methods. In C.R.A. Catlow, editor, *Computer Modeling in Inorganic Crystallography*, pages 83 – 115. Academic Press, London, 1997.

[30] J. H. LaCasce. The prevalence of oceanic surface modes. *Geophysical Research Letters*, 44(21):11,097–11,105, 2017.

[31] Marta Sanchez de La Lama, J H LaCasce, and Helle Kristine Fuhr. The vertical structure of ocean eddies. *Dynamics and Statistics of the Climate System*, 1(1), 09 2016. dzw001.

[32] J. H. LaCasce and Sjoerd Groeskamp. Baroclinic modes over rough bathymetry and the surface deformation radius. In progress, 2020.

[33] Dudley B. Chelton, Roland A. deSzoeke, Michael G. Schlax, Karim El Naggar, and Nicolas Siwertz. Geographical variability of the first baroclinic Rossby radius of deformation. *Journal of Physical Oceanography*, 28(3):433–460, 03 1998.

[34] Musa H., Ibrahim Saidu, and Marianus Waziri. A simplified derivation and analysis of fourth order Runge Kutta method. *International Journal of Computer Applications*, 9, 11 2010.

[35] J. I. Antonov O. K. Baranova C. Coleman H. E. Garcia A. Grodsky D. R. Johnson R. A. Locarnini A. V. Mishonov T.D. O'Brien C.R. Paver J.R. Reagan D. Seidov I. V. Smolyar Boyer, T.P. and M. M. Zweng. *NOAA Atlas NESDIS*, 72:209, 2013.

[36] Carl Wunsch. The vertical partition of oceanic horizontal kinetic energy. *Journal of Physical Oceanography*, 27(8):1770–1794, 08 1997.

[37] Peter Rhines and Francis Bretherton. Topographic Rossby waves in a rough-bottomed ocean. *Journal of Fluid Mechanics*, 61(3):583–607, 1973.

Acknowledgements

I want to thank Femke de Jong and Sjoerd Groeskamp for the excellent supervision of this internship. It was great to work together with both of you. The cooperation has been very encouraging, effective and pleasant, and I could always ask my questions. We had to work from home due to the Corona pandemic, which, however, did hardly affected our progress. Femke, thank you for allowing me to join the OSNAP research cruise, it was an incredible experience. Sjoerd, thank you for coming up with the idea for this internship and all the enthusiasm you put into it.

Further on, I would also like to thank Nora Fried for helping me with the mooring data. You always had a critical look at the results, which has undoubtedly helped us forward.

I would also like to thank Gertjan van Heijst and Matias Duran Matute for acting as supervisors from the university.

The internship was a challenging, educational and rewarding experience. Thank you all for the positive energy and good luck in your further research.

Appendix A

Mooring comparison weekly mesoscale mixing

This section contains the results of the weekly derived mesoscale mixing for each mooring separately. Figure A.1 shows the eddy deformation length L_d, fig. A.2 the unsuppressed mesoscale mixing K_{MLT}, fig. A.3 the suppression factor $S_\perp$ and fig. A.4 the suppressed mesoscale mixing $K_\perp$. The results of the weekly mesoscale mixing are discussed in section 4.3.

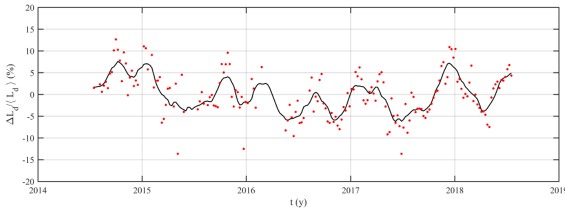

(a) *IC1*, $\langle L_d \rangle$ *= 12.3 km*

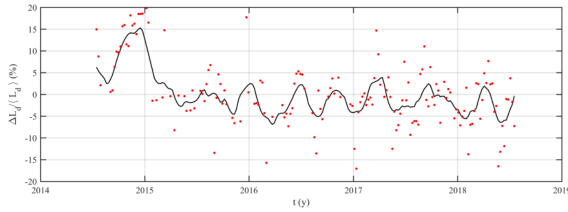

(b) *IC2*, $\langle L_d \rangle$ *= 10.8 km*

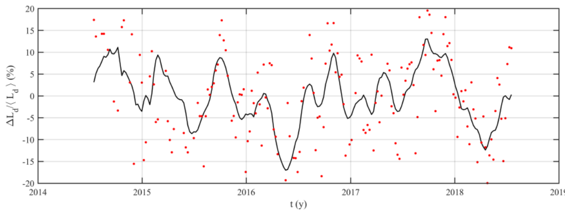

(c) *IC3*, $\langle L_d \rangle$ *= 10.3 km*

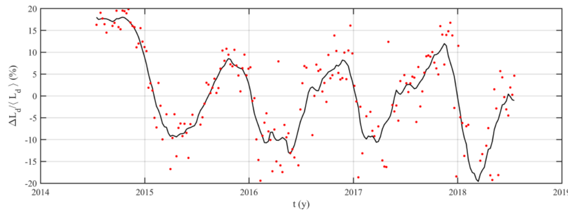

(d) *IC4*, $\langle L_d \rangle$ *= 11.1 km*

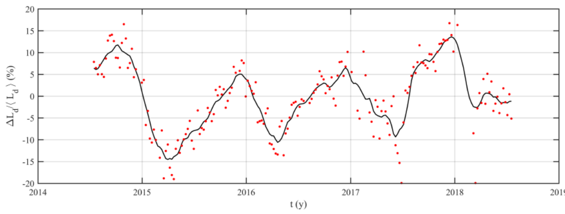

(e) *M1*, $\langle L_d \rangle$ *= 12.1 km*

Figure A.1: *Deformation radius as function of time per mooring on a weekly basis. The average deformation radius per mooring is indicated in the caption.*

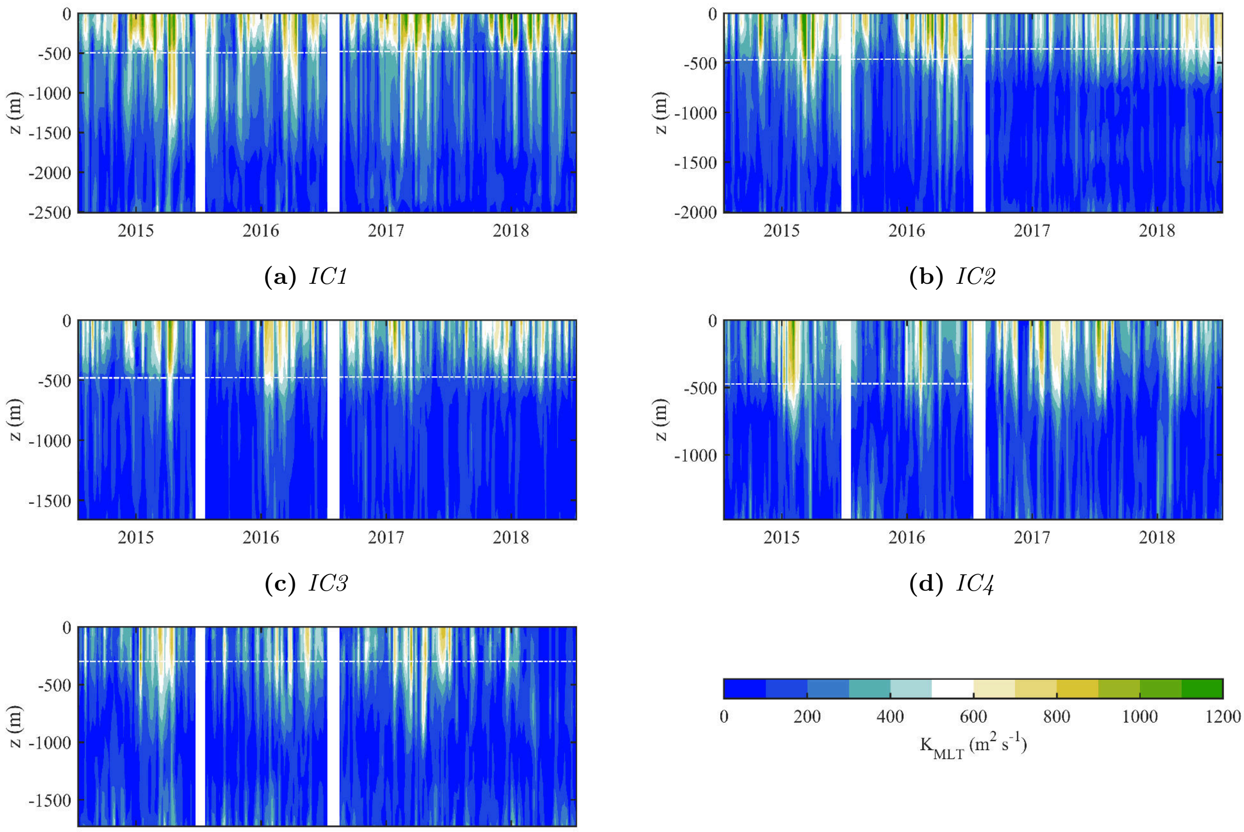

(a) *IC1*

(b) *IC2*

(c) *IC3*

(d) *IC4*

(e) *M1*

Figure A.2: *Overview of unsuppressed mixing per mooring on a weekly basis.*

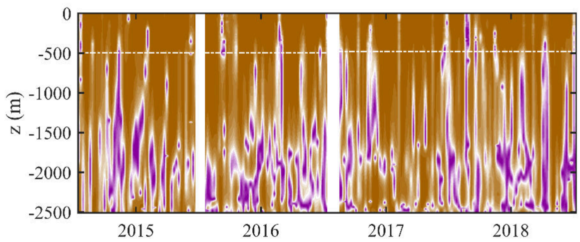

(a) *IC1*

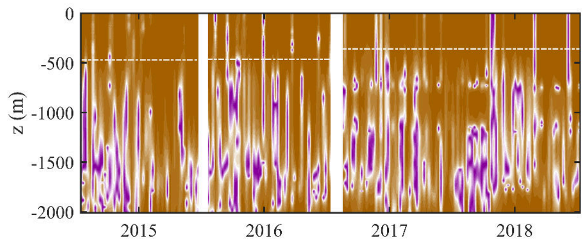

(b) *IC2*

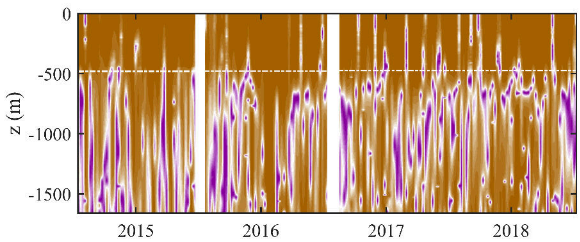

(c) *IC3*

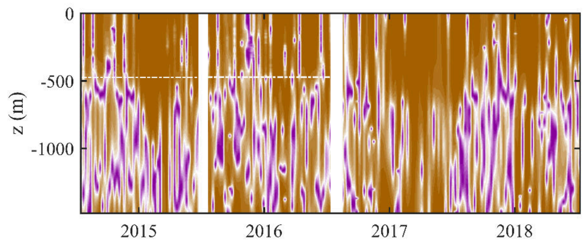

(d) *IC4*

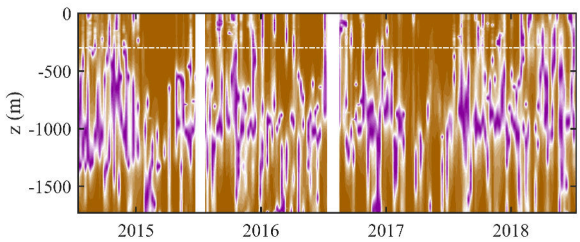

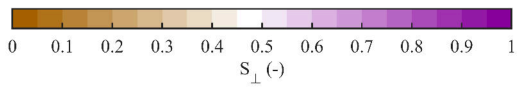

(e) *M1*

Figure A.3: *Overview of suppression component $S_\perp$ per mooring on a weekly basis.*

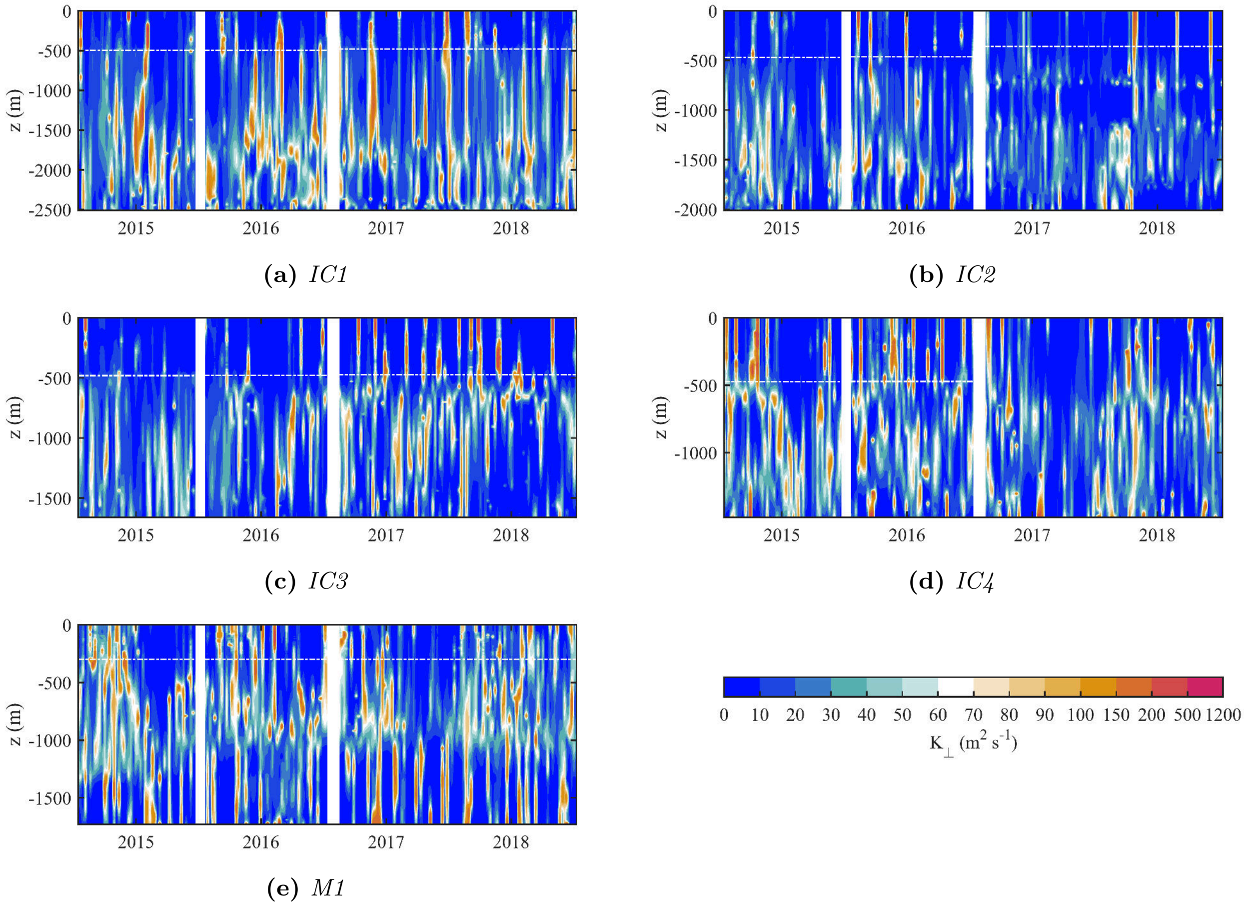

Figure A.4: *Overview of the cross-current component of the suppressed mesoscale mixing per mooring on a weekly basis.*